SLAC-R-608

Large Bulk Matter Search for Fractional Charge Particles*

I. T Lee

Stanford Linear Accelerator Center
Stanford University
Stanford, CA 94309

SLAC-Report-608
December 2002

Prepared for the Department of Energy
under contract number DE-AC03-76SF00515

Printed in the United States of America. Available from the National Technical Information Service, U.S. Department of Commerce, 5285 Port Royal Road, Springfield, VA 22161.

*Ph.D. thesis, Stanford Linear Accelerator Center OR Stanford University, Stanford, CA 94309.

LARGE BULK MATTER SEARCH FOR FRACTIONAL CHARGE PARTICLES

A DISSERTATION
SUBMITTED TO THE DEPARTMENT OF PHYSICS
AND THE COMMITTEE ON GRADUATE STUDIES
OF STANFORD UNIVERSITY
IN PARTIAL FULFILLMENT OF THE REQUIREMENTS
FOR THE DEGREE OF
DOCTOR OF PHILOSOPHY

Irwin T Lee
December 2002

I certify that I have read this dissertation and that, in my opinion, it is fully adequate in scope and quality as a dissertation for the degree of Doctor of Philosophy.

Martin Perl
(Principal Advisor)

I certify that I have read this dissertation and that, in my opinion, it is fully adequate in scope and quality as a dissertation for the degree of Doctor of Philosophy.

Su Dong

I certify that I have read this dissertation and that, in my opinion, it is fully adequate in scope and quality as a dissertation for the degree of Doctor of Philosophy.

John Jaros

Approved for the University Committee on Graduate Studies:

Abstract

We have carried out the largest search for stable particles with fractional electric charge, based on an oil drop method that incorporates a horizontal electric field and upward air flow. No evidence for such particles was found, giving a 95% confidence level upper limit of 1.17×10^{-22} particles per nucleon on the abundance of fractional charge particles in silicone oil for $0.18e \leq |Q_{residual}| \leq 0.82e$. Since this is the first use of this new method we describe the advantages and limitations of the method.

Acknowledgments

I am deeply indebted to my advisor, Martin Perl, for his guidance throughout the past several years. His oversight of the experiment as well as over my struggles with classwork was indispensable. His enthusiasm for research is unmatched in anyone I have met, as is his endless drive. This dedication to the experiment and science in general made it a pleasure to study under him.

Working as a member of our small research group was a truly enjoyable experience because of our diversity in interests, skills, and background. Thanks are due to the entire group, particularly Dinesh, Peter, Howard, and Sewan, from each of whom I've learned a great deal. Of course, I was very fortunate to work with Valerie and Eric, who made our office, by a large margin, the most interesting office at SLAC, as well as the most politically incorrect workspace in the free world.

I am grateful to Judy Meo for being helpful in all things, and Lilian DePorcel for being able to accomplish bureaucratic impossibilities. The time taken out of busy schedules by Su Dong, John Jaros, Giorgio Gratta, and Amos Nur to serve on my examination committee is also appreciated.

Finally, I cannot say enough to thank my parents, who made all of this possible. For their efforts, I have had more opportunities and fewer worries than practically anyone.

Contents

List of Tables

List of Figures

Chapter 1

Introduction

In the Standard Model of particle physics, electric charge is quantized in units of e, the electron charge. No particles with non-integral (fractional) charge have ever been observed in isolation.

Of course, Standard Model quarks do carry fractional electric charge, but they are always bound together in combinations with integral charge. Strictly speaking, quarks are believed to be constrained to be bound together in combinations with zero net *color*, which is the confinement hypothesis, but one of the features of the Standard Model is an apparent correlation between colorless states and states with integer charge. This confinement hypothesis cannot be directly proven despite the fact that the Lagrangian for the strong interaction between quarks is known, since the calculations involved are too difficult. Computer simulations have confirmed that confinement holds up to very high energies, and no isolated quarks have been observed in accelerator experiments. The remaining possibilities for finding isolated quarks include finding relic free quarks created during the early formation of the universe, or finding one as a product of an extremely high energy interaction, such as one involving cosmic rays.

Other candidates for fractional charge particles (FCPs) come from physics beyond the Standard Model, where they are a common occurrence in theoretical physics. It is often claimed, for example, that if supersymmetry is correct, there must be stable, fractional charge particles in addition to the particles already observed. On a less

theoretical footing, the experimental evidence for dark matter possibly points to the existence of a new fundamental particle making up a significant portion of the mass of the galaxy. Recent papers have shown that it is possible for charged particles to remain uncondensed in the galactic halo if they are sufficiently massive (CHAMPS). The properties, including the charge, of such a particle are of course totally unknown.

Previous experiments have constrained such speculation primarily for relatively light particles. Since FCPs by definition are charged, it must be possible to pair produce them through the electromagnetic interaction. Cosmic ray and accelerator based searches have indeed directly looked for the production of FCPs. The null result from these experiments constrains any hypothetical FCP to large masses unreachable by existing accelerators, or possibly to having such small cross sections for production that such an event has not been observed.

Previous bulk matter searches have limited the abundance of FCPs to less than $\sim 10^{-21}$ particles per nucleon. However, because of the specific techniques involved, it is a continuing weakness of these experiments that only very specific materials, and typically not particularly interesting ones, have been studied. The overall strategy for this work is to make possible the search in a variety of materials which for one reason or another are thought to be good candidates for having FCP as inclusions, and maximizing the throughput of those materials.

1.1 The experiment

We have carried out the largest search for fractional electric charge elementary particles in bulk matter using 70.1 mg of silicone oil. That is, we looked for stable particles whose charge Q deviates from Ne where N is an integer, including zero, and e is the magnitude of the charge on the electron. No evidence for such particles was found in this amount of silicone oil. We used our new version [10] of the Millikan oil drop method containing two innovations compared to the classical method that we used in Halyo *et al.*[2]. One innovation is that the drop charge is obtained by observing the drop motion in a *horizontal*, alternating electric field compared to the classical use of a vertical electric field [2, 11, 14]. The other innovation is the use of an upward flow

of air to reduce the vertical terminal velocity of the drop, which enabled us to use larger drops, about 20.6 μm in diameter compared to the 10 μm drops used in our previous experiments.

We define the residual drop charge, $Q_r = Q - N_l e$ where N_l is the largest integer less than Q/e. We find the 95% confidence level upper limit on the abundance of fractional charge particles in silicone oil for $0.18e \leq Q_r \leq 0.82e$ is 1.17×10^{-22} particles per nucleon. This experiment was a follow up on our previous search in silicone oil, Halyo *et al.*[2], based on 17.4 mg. In that search we found one drop with anomalous charge, but no such charge was found in the present experiment.

In this thesis, I describe the experimental method and apparatus in Sec. 2. The data acquisition system and software are covered in Sec. 3. In Sec. 5 we discuss the measurement precision resulting from the various measurement errors and the calibration methods. The data analysis method, including the criteria used to accept drop charge measurements, is discussed in Sec. 6. Here we pay particular attention to the drop spacing criterion necessitated by interactions between adjacent drops. This is the primary limitation on the rate at which drops can be measured and we had to acquire considerable experience to understand this limitation. We conclude with Sec. 7, giving our results, comparing our results with other fractional charge searches, and discussing the applicability and extension of this new Millikan oil drop technique to other searches.

Chapter 2

Experimental method and apparatus

2.1 Experimental method

The principle of the experimental method is simple. Consider a drop of radius r, density ρ, and charge Q falling in air through a horizontal electric field of strength E, as shown in Figure 2.1. The coordinate system is chosen such that the drop falls in the positive z direction, the x axis is parallel to the electric field and pointing towards the grounded capacitor plate, and the y axis is such that the resulting coordinate system is right handed.

Applying Stokes' law the horizontal terminal velocity, v_x is

$$v_x = \frac{QE}{6\pi\eta r} \tag{2.1}$$

where η is the viscosity of air. Hence measuring v_x gives Q providing r is known. As explained in Sec. 5.1, the drop radius is determined from the v_x of integer charge particles. Note that the measurement of Q does not depend on the density of the drop and is also independent of the gravitational force on the drop. The electric field alternates in the $+x$ and $-x$ direction so that the drop is moved back and forth along the x axis. This cancels some sources of error and allows the drop motion to

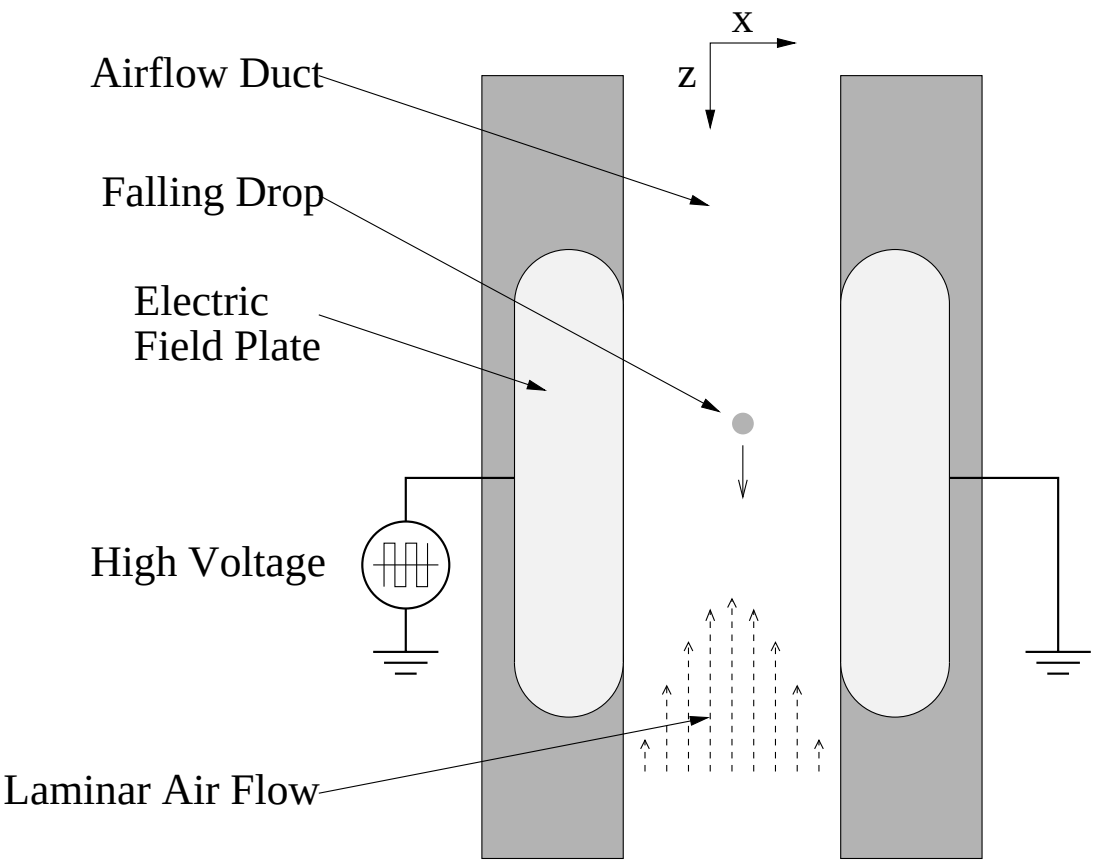

Figure 2.1: Basic principles of the experimental method.

be viewed in a relatively narrow horizontal area. Previous uses of a static horizontal electric field in the Millikan oil drop method were in 1941 by Hopper and Laby [3] who measured the electron charge and by Kunkel [5, 6] in 1950 who measured the charge on dust particles.

If the drop were falling in still air, the vertical terminal velocity would be given by

$$v_{z,term} = \frac{2r^2\rho g}{9\eta} \tag{2.2}$$

where g is the acceleration of gravity. However we use an upward flow of air of velocity v_{air} in the $-z$ direction. Hence the net downward velocity of the drop is

$$v_z = \frac{2r^2\rho g}{9\eta} - v_{air}. \tag{2.3}$$

As explained in the next section we want v_z to be small hence we set v_{air} to be close to $v_{z,term}$ but slightly smaller.

2.2 General description of experiment

Figure 2.2 is a schematic picture of the apparatus. Drops averaging 20.6 μm in diameter are produced at a rate of 1 Hz using a piezoelectrically actuated drop-on-demand microdrop ejector. The drops fall through the upward moving air in the measurement chamber passing through a horizontal, uniform, alternating electric field. In this figure the electric field is perpendicular to the paper. The electric field alternates as a square wave with a frequency of 2.5 Hz and has an amplitude of about 1.8×10^6 V/m.

A rectangular measurement region 2.29 mm in the x direction by 3.05 mm in the z direction is projected by a lens onto the charge-coupled device (CCD) sensor of a monochrome, digital video camera. A light source consisting of a bank of light emitting diodes (LEDs) provides 10 Hz stroboscopic illumination. As the motion of the drop carries it through the measurement region, its image appears on the surface of the CCD. Thus the camera collects 10 frames per second, the drop appearing as a

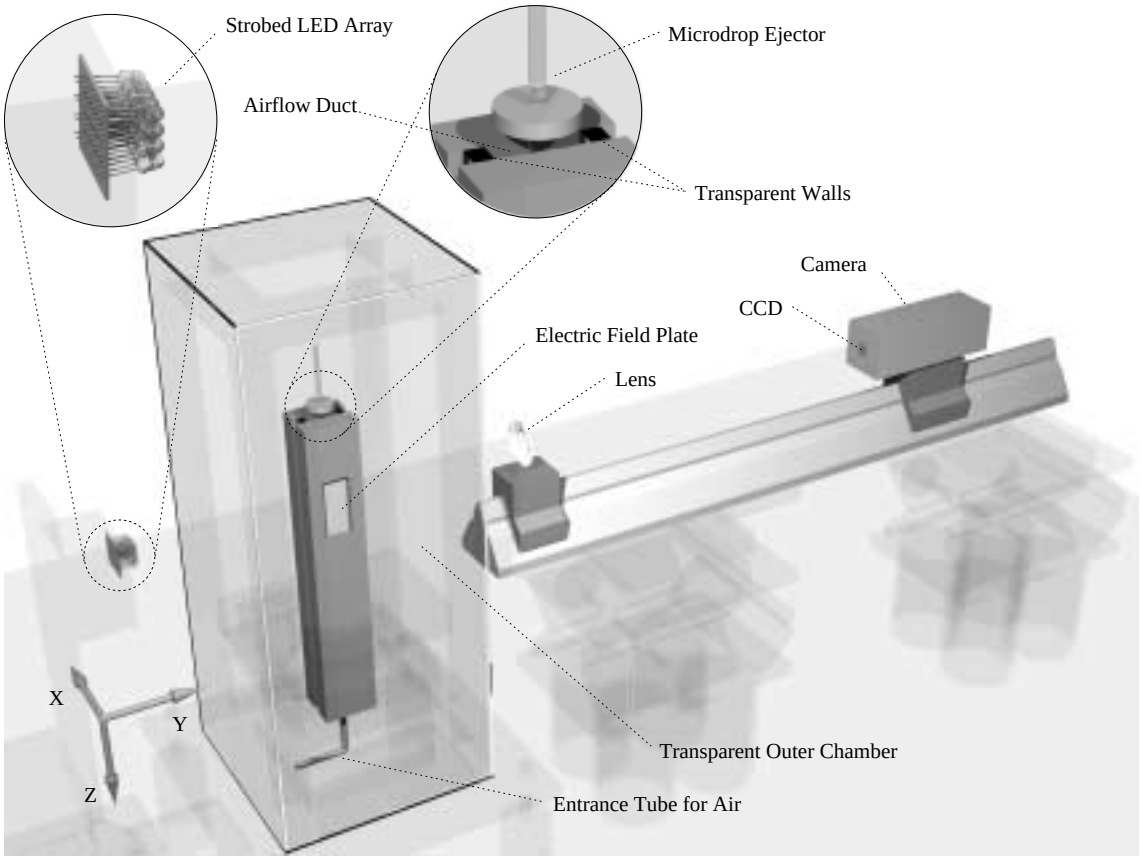

Figure 2.2: Diagram of the apparatus. Diagram is to scale, except for the lens and CCD which are shown at 2× scale. Support structures are drawn transparent for clarity.

dark image on a bright background.

In addition to the v_x motion there is also the v_z motion, Eq. (2.3). Since the camera has a field of view of $Z = 3.05$ mm in the vertical direction, the 10 Hz stroboscopic illumination leads to acquisition of

$$N_{images} = 10Z/v_z = 30.5/v_z \tag{2.4}$$

images of any given drop, as the drop moves through the viewing area of the camera. Here v_z is in mm/s. Hence we get a larger number of images per drop, leading to better charge measurement precision, when v_z is small. Of the order of $N_{images} = 15$ are required.

We give an example of the importance of the upward airflow in obtaining this many images. Consider a typical drop of diameter 20.6 μm with a density of 0.913 g/cm^3. From Eq. (2.2), $v_{z,term} = 11.3$ mm/s. If there were no upward airflow there would be an average of 2.6 images per drop. To obtain $N_{images} = 15$, v_z must be about 2.0 mm/s. Therefore from Eq. (2.3), v_{air} must be $11.3 - 2.0 = 9.3$ mm/s.

Each image from the CCD camera is processed though a framegrabber in a conventional desktop computer, the signal in each pixel being recorded. An analysis program then finds the drop images and calculates the x and z coordinates of the centroid of the drop image. Using all the images of the drop and knowing the time spacing of the images, v_x and v_z are then calculated.

2.3 Drop generator

The drop generator, Figure 2.3, is based on the general design principles used in piezoelectrically actuated, drop-on-demand, inkjet print heads. Our generator is designed for flexibility, allowing a variety of liquids to be used and providing ease of control and maintenance. The body of the generator is glass so as to preserve the purity of the liquid, but the ejection aperture at the bottom is micromachined silicon [9]. The diameter of the aperture sets approximately the diameter of the drop. Upon application of a short voltage pulse, usually 3 to 20 μs, across the surfaces of the

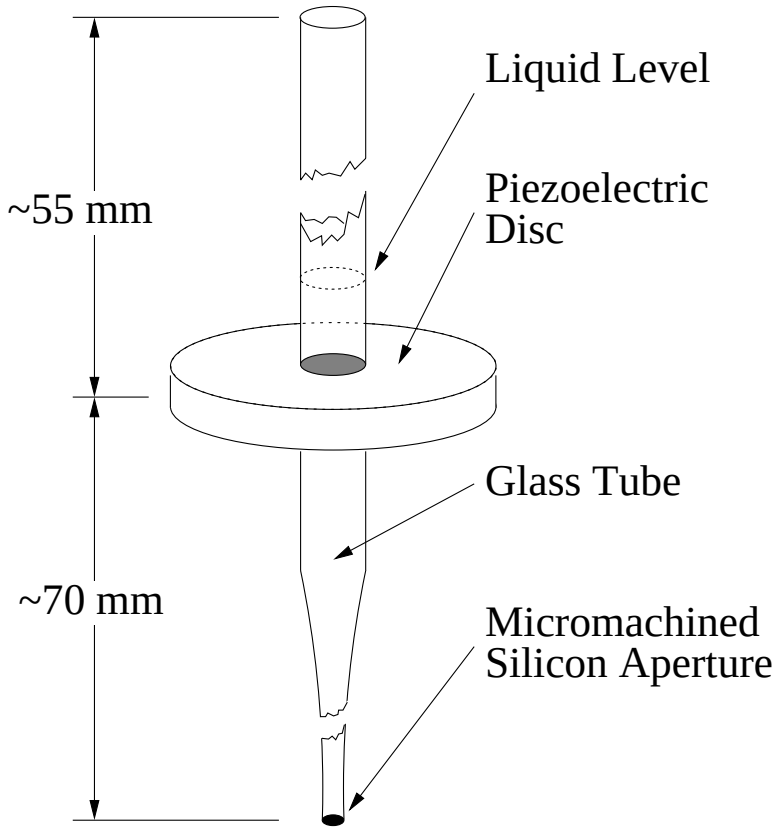

Figure 2.3: Drop generator.

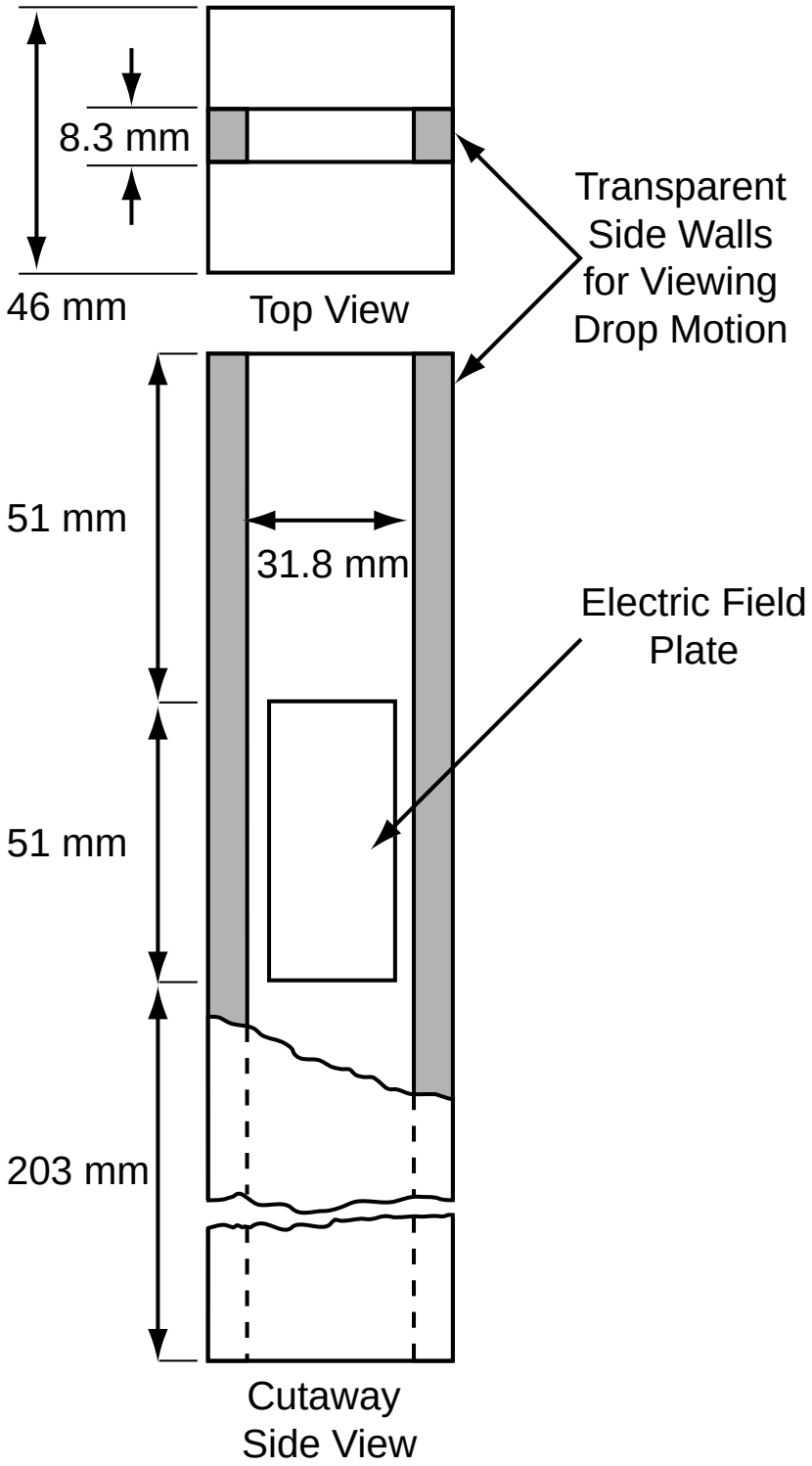

Figure 2.4: Airflow tube and measurement chamber.

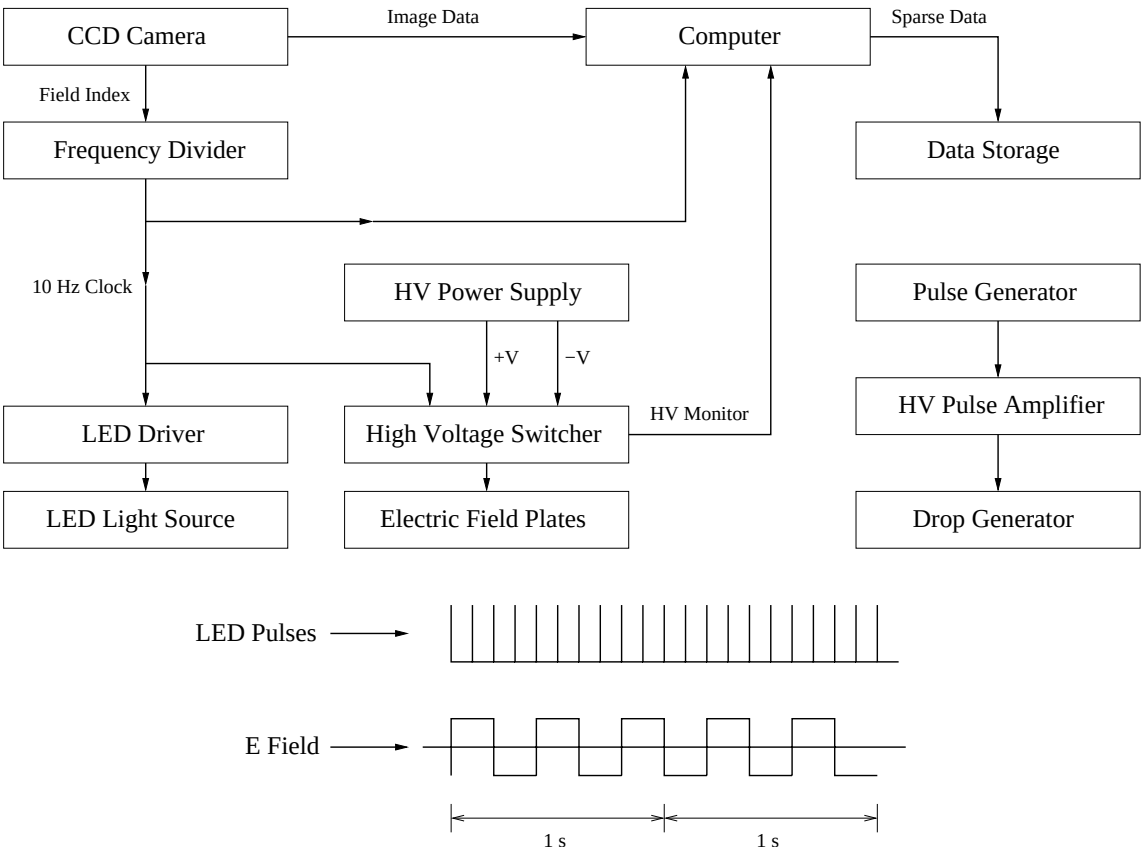

Figure 2.5: Schematic of electronic system. The LED and high voltage is synchronized to the 10 Hz clock, while the drop generator runs asynchronously.

piezoelectric disk, the central hole in the disk contracts in diameter, squeezing the glass tube and sending a pressure pulse down the liquid, ejecting a jet of fluid from the aperture. The forming of a discrete fluid drop from the high speed jet is a complex process with the repeatability of the process and the final diameter of the drop being highly dependent on the properties of the fluid, and on how the fluid is driven. For this reason, the shape and amplitude of the voltage pulse applied to the piezoelectric disk must be specifically tuned for stability and the desired drop size. In addition, it is necessary to experiment with single and double pulsing, varying both the pulse width and the separation between the pulses.

The pressure in the drop generator is maintained slightly below atmospheric pressure by 10 to 30 mm Hg. This helps to retract the excess liquid outside the ejection aperture after the drop has been produced and also prevents leaking of the liquid between pulses.

It is important that the drop generator produce drops of constant radius, the primary reason being that the size of the drops determines the ratio between Q and the measured quantity v_x, from Eq. (2.1). A secondary reason that we did not initially appreciate has to do with Eqs. 2.2 and 2.3. We set v_{air} close to $v_{z,term}$ so that v_z is much smaller than $v_{z,term}$. Thus a small change in r leads to a relatively large change in v_z. This dispersion disrupts the consistent spacing between adjacent drops, and a decreased separation between drops is undesirable for reasons discussed in Sec. 6.1.6.

With a clean and newly tuned drop generator we get remarkably uniform drop radii, constant to about $\pm 0.2\%$. The drop generator also ejects in a consistent downward vertical direction along the centerline of the airflow tube. At 1 Hz operation, the drop ejector exhibits slow drifts in its characteristics with time scales of the order of a week. These drifts appear as changes in drop size and as destabilization that manifests as the appearance of satellite drops or inconsistent drop production. Typically, these effects can be compensated for by small changes in the drive parameters or adjustments of the air velocity or both. By the end of the first data set, set 1, the drop ejector had destabilized to the point where it had to be removed from the apparatus for cleaning and refilling. Similarly during the taking of data set 2, the drop ejector and air velocity required periodic small adjustments. The end of set 2 was

caused by increasing instability in drop production which could not be compensated for. We do not know the reason for this behavior.

In our drop generator the silicone oil drops are produced with a spread of charges, $|Q|$ ranging mostly from 0 to about 10 e. A few percent of the drops have larger $|Q|$. As described in Sec. 6.1.1 we used drops with $|Q| < 9.5e$ to maintain good precision in the charge measurement. We do not know what sets the charge distribution for a particular drop generator. But we have the general observation that silicone oil gives narrow charge distributions, whereas water, mineral oil and most other organic liquids give broad charge distributions, with $|Q|$ values as large as several 1000 e or even larger.

2.4 Optical system

Referring to Figure 2.2, the stroboscopic light source consists of a rectangular bank of 20 LED's emitting at 660 nm. The pulse length was about 100 μs. The lens, a 135 mm focal length, $f/11$, photographic enlarging lens, images the measurement region onto the face of the CCD camera with a magnification of 2.1.

The rectangular active image area of the CCD camera, a Cohu 4110 with RS-170 and digital output, is 4.8 mm in the horizontal, that is, x, direction, and 6.4 mm in the vertical, that is, z, direction. Hence the viewing area in physical space is 2.29 mm horizontally by 3.05 mm vertically. We remind the reader that the electric field is horizontal. The active imaging area is an array of 240 horizontal picture elements (pixels) and 736 vertical picture elements (pixels). We chose this orientation of the array to maximize the vertical distance, maximizing the number of images per drop.

Given the magnification and pixel density of the CCD, one would expect from geometric optics that the shadow of a 20 μm diameter drop would cover 2 pixels horizontally and 5 pixels vertically. The actual observed shadow typically covered 3 pixels horizontally and 7 pixels vertically, and had an intensity variation that was approximately a two dimensional Gaussian. This can be quantitatively described as the convolution of the simple shadow predicted by geometric optics with a point spread function that is a result of the diffractive effects due to the finite aperture of

the lens. We do not and should not observe diffractive effects caused by the small size of the drops.

2.5 Airflow tube and measurement chamber

Figure 2.4 shows a slightly simplified, dimensioned drawing of the airflow tube and the measurement chamber. A rectangular duct contains the upward flowing air. It is 8.3 mm wide in the direction of the electric field and 31.8 mm wide in the direction perpendicular to the electric field. The field plates that define the measurement chamber are 51 mm high and 28.6 mm wide. The inner surfaces of the plates are machined flat and are in the same plane as the inner surfaces of the walls of the airflow tube. The optic axis of the optical system passes through the transparent side walls of the airflow tube.

The air velocity is sufficiently small, with a Reynolds number on the order of $R_e = 50$ so that the flow is laminar. The 203 mm length of air flow tube between the measurement region and the air inlet allows the air to settle into its equilibrium flow pattern. At equilibrium, the velocity profile of the air is approximately parabolic across the narrow direction of the channel (x axis). Across the long axis, the flow has a roughly constant central region and falls to zero at the boundaries [7].

2.6 Electronics

All the electronics of the apparatus, Figure 2.5, are hard-wired to give reliable timing, independent of the operation of the computer. A 30 Hz handshaking signal from the CCD is divided down to provide a 10 Hz clock that synchronizes the LED strobe, the electric field switcher and the computer image acquisition. The switching of the electric field, which is driven by the clock signal divided by 4, operates at 2.5 Hz. This results in a cycle where two images are acquired with the electric field in one direction, and then two images with the electric field in the other direction. These relationships between the signals is depicted in the timing diagram of Figure 2.5. The drop generator is driven asynchronously at 1 Hz.

Chapter 3

Software and data acquisition

Data acquisition was performed by a single desktop computer running Linux. The computer was equipped with two special components: a digital framegrabber that allowed the capture of image data from the camera and a general purpose input/output interface board with digital I/O and A/D conversion capability. The additional inputs allowed the computer to monitor the state of the experiment as well as a variety of environmental variables.

All software was custom written in C. Hardware dependent code was encapsulated into drivers at the kernel level, which allowed a guarantee of synchronization of the software with apparatus by a combination of hardware and software buffering of the data.

The overall strategy was to acquire data from the apparatus and write them to files in *raw* form for later processing off line. Recall that each image frame contains 736×240 pixels, each digitized to 8 bit accuracy. Therefore acquiring data at 10 Hz produces a data rate from the CCD camera of about 2 MB/s, much too large to be stored. Since an image contains just a few drops, most of the pixels in an image have just the background signal, which allows the information to be stored using sparse storage. As mentioned in Sec. 2.4, the typical image of drop extends over an area of 3 pixels by 7 pixels. In each frame the regions containing drops were isolated using a thresholding operation. The position of each drop was then measured using a simple center of mass algorithm, and for each drop only a surrounding region containing 13

horizontal pixels by 21 vertical pixels of the image is written to the output file.

Chapter 4

Data collection

The search was carried out in two sets described in Table 4.1.

Table 4.1: Data collection

Data set	Days	Number of drops	Total mass (mg)
1	75	3 377 477	12.1
2	186	13 430 167	58.0

The drop ejector used in Set 1 was built around a 30 μm square micromachined orifice, which was tunable for drops in the 20 μm range. The drop ejection rate, in terms of mass ejected per day, is shown in Figure 4.1.

At the beginning of the Set 1 the drop ejector was operated at 0.5 Hz. The sudden increase in rate at approximately day 20 is due to doubling of the ejection rate to 1 Hz, which was maintained for the remainder of Set 1. The irregularities at approximately day 56 were due to shutdowns for various hardware and software installation. The actual mass throughput successfully analyzed is shown in Figure 4.2.

The steady decrease in analyzed mass throughput was a result of increasing amounts of data being discarded by selection criteria during analysis, primarily due to drops approaching each other too closely. This selection criteria is explained in depth in Sec. 6.1.6. Since the drops are produced at equal intervals and are therefore initially evenly spaced as they fall through the chamber, the increase in close

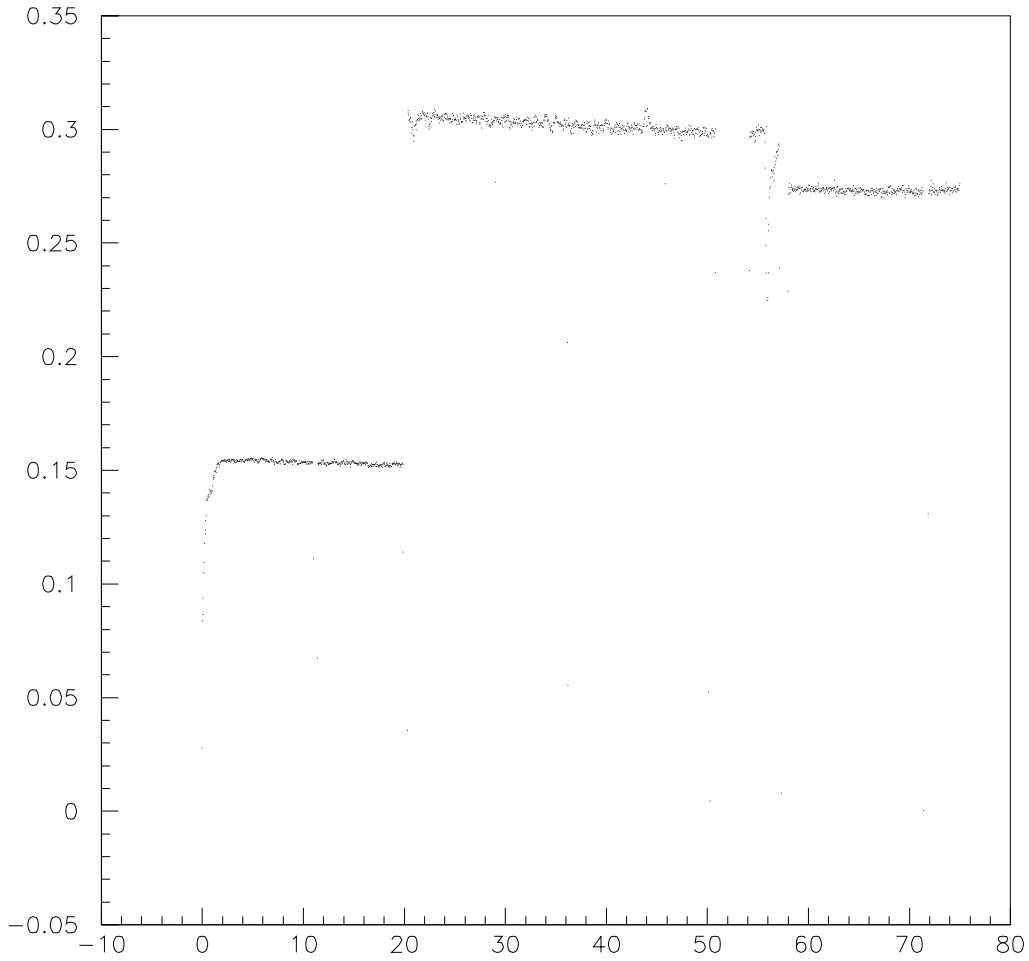

Figure 4.1: Raw mass throughput rate in apparatus as a function of time for data Set 1. The rate is shown in units of mg per day, where time is indicated in days starting from the beginning of the run.

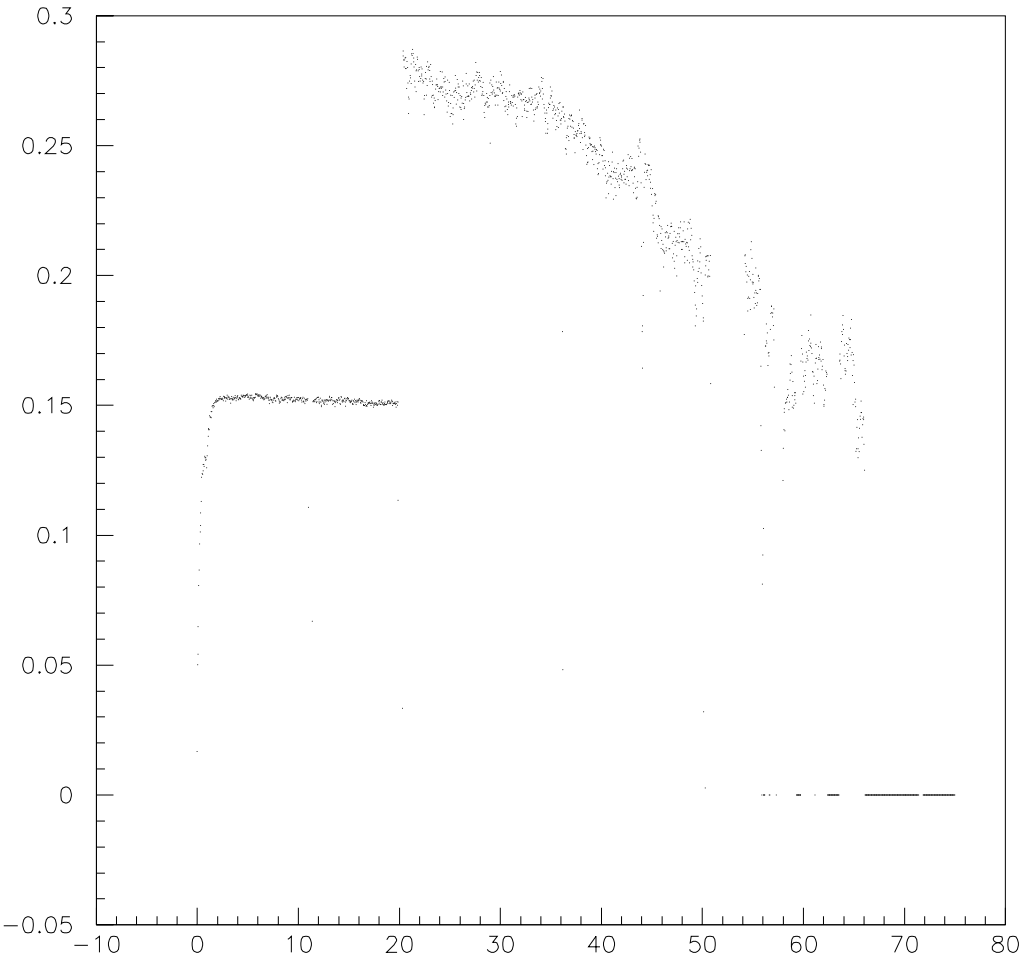

Figure 4.2: Analyzed mass throughput rate in apparatus as a function of time for data Set 1. The rate is shown in units of mg per day, where time is indicated in days starting from the beginning of the run.

approaches between drops is an indicator of irregularity in the drop ejection process. These irregularities manifest as an increased spread in the size of the drops, as well as increased scatter in their x positions. Both irregularities increase the scatter in the velocity of the drops through the apparatus, through variations in the terminal velocity and variations in the velocity of the airflow, respectively. The percentage of drops rejected due to close approaches to another drop is shown in Figure 4.3, while the gradual increase in x position fluctuations is shown in Figure 4.4.

The drop ejector was constantly monitored, and its parameters were occasionally adjusted to optimize drop production. The irregularities shown gradually increased despite these maintenance procedures, and after 75 days it was no longer possible to take good data using that particular drop ejector. After removal from the apparatus and inspection, it was discovered that the micromachined orifice of the drop ejector had gradually been sustaining damage, and required replacement.

The new drop ejector constructed for data Set 2 was based on a 20 μm square micromachined orifice, and incorporated an additional modification from the previous ejector in that the pipette was elongated using glass-blowing techniques. This modification allowed the drops to be injected into the chamber closer to the actual measurement region, tending to make the spacing between drops more uniform. While drops were always produced at 1 Hz during the collection of data Set 2, slow drifts in the drop size produced caused some variation in the raw mass throughput, as shown in Figure 4.5. As before, increasing instability in drop production eventually caused a rapid drop in the quality of the data collected, as is indicated in Figure 4.6 by the rapid decrease in analyzed mass throughput towards the end of the run. Again, as before, inability to produce mono-disperse drops caused the end of data collection.

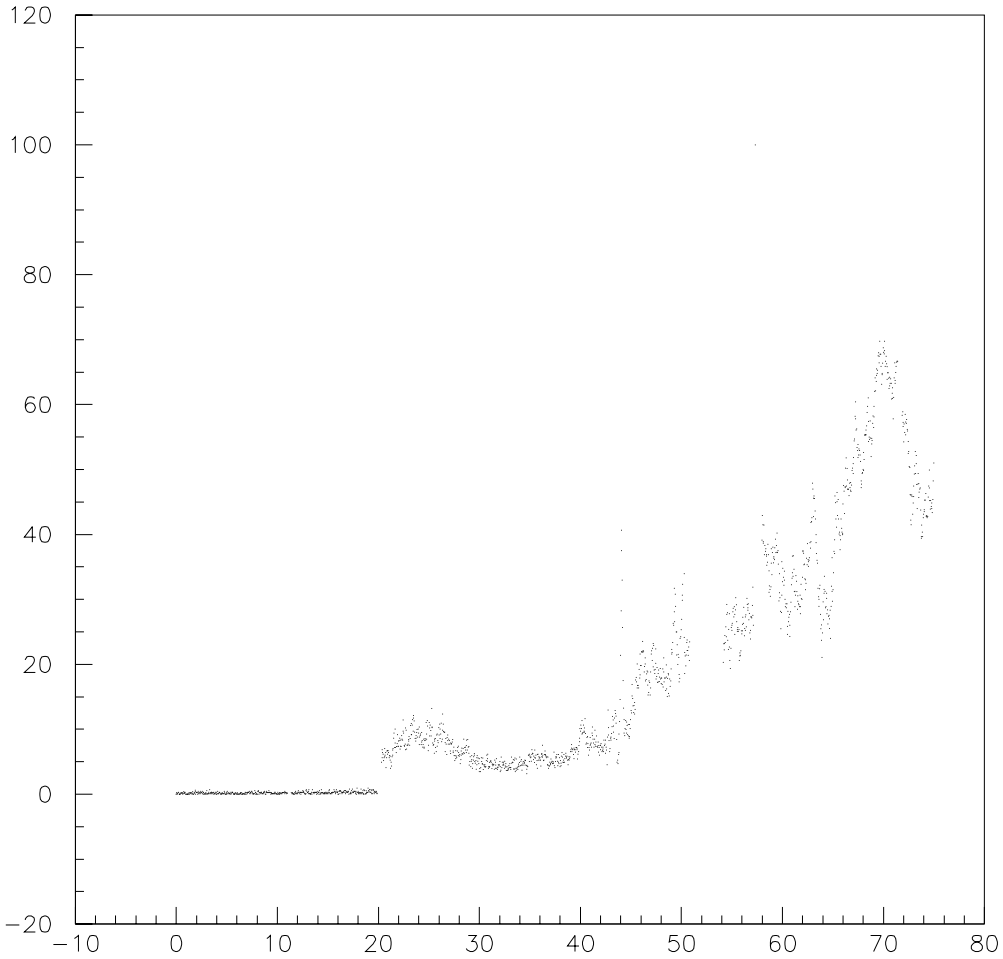

Figure 4.3: The percentage of drops rejected by selection criteria during analysis, for approaching another drop in the chamber too closely, as a function of time (in days) for data Set 1.

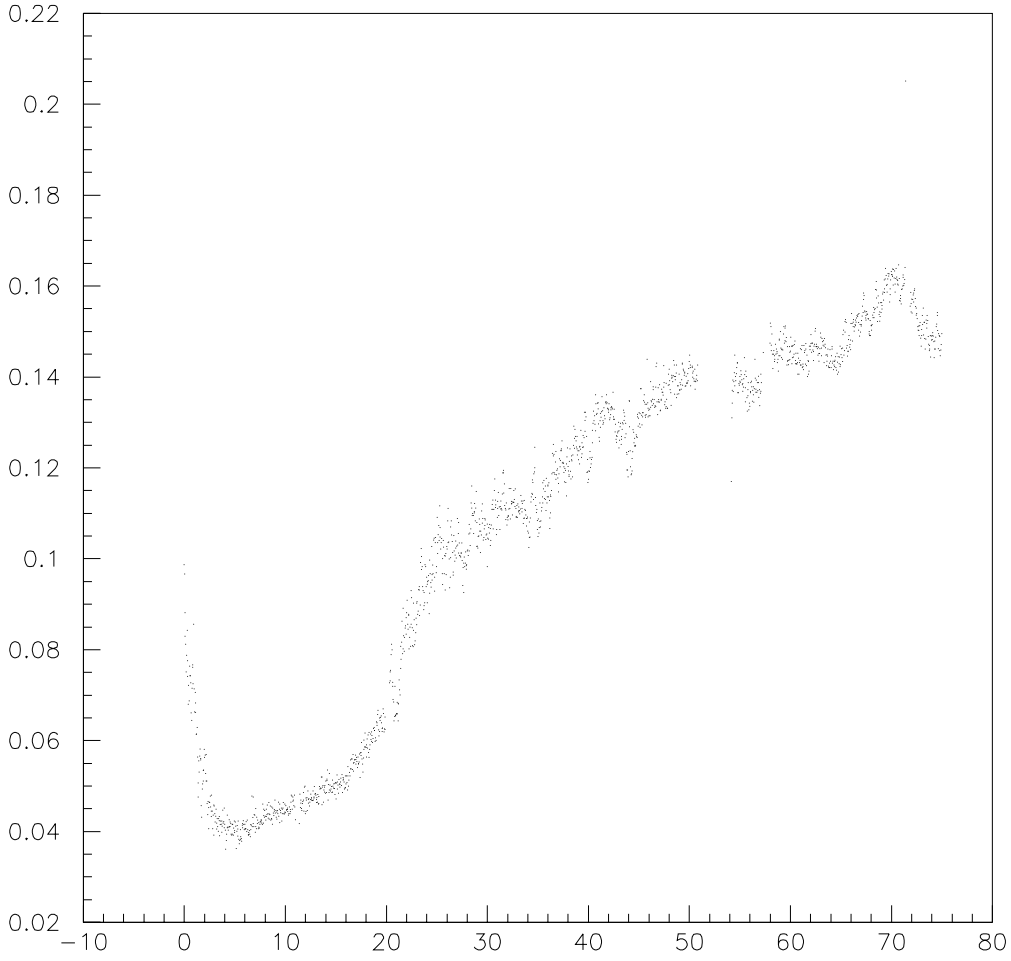

Figure 4.4: The rms of the fluctuations in the x positions of the drops (in mm) as a function of time (in days) for data Set 1.

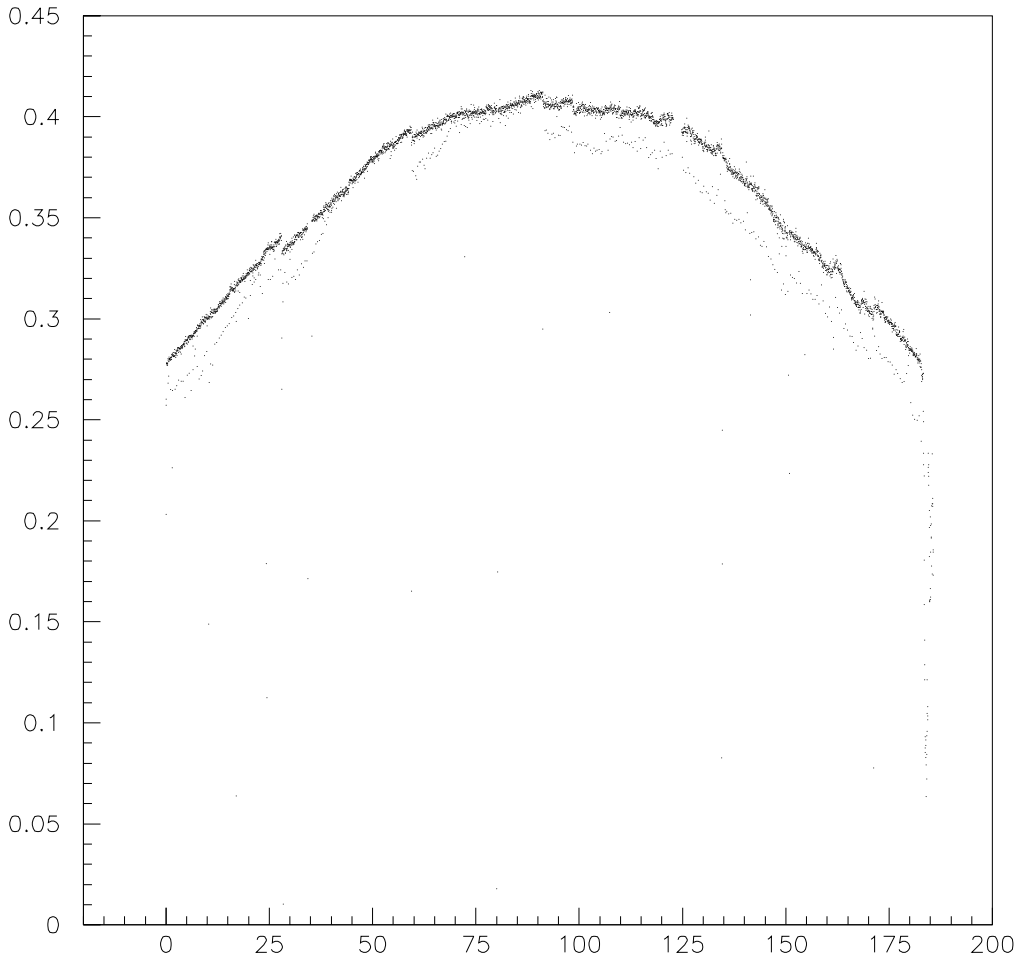

Figure 4.5: Raw mass throughput rate in apparatus as a function of time for data Set 3. The rate is shown in units of mg per day, where time is indicated in days starting from the beginning of the run.

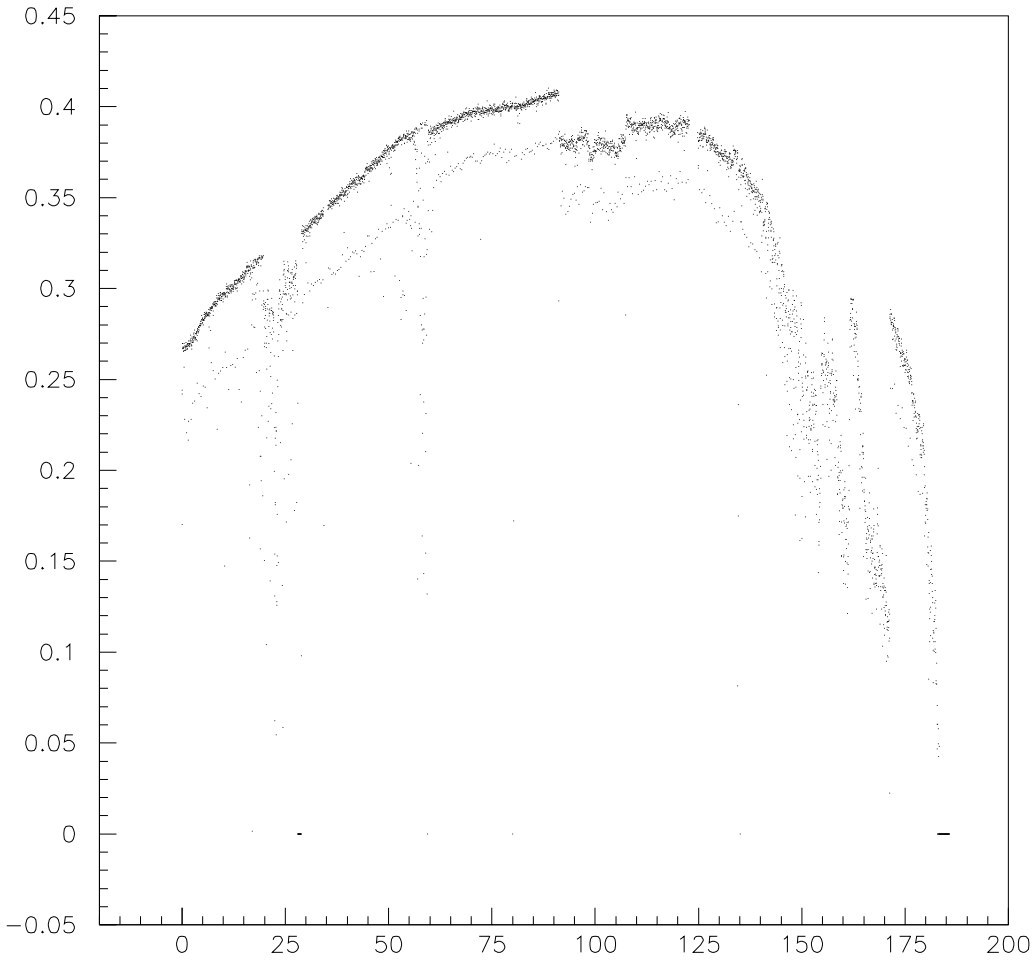

Figure 4.6: Analyzed mass throughput rate in apparatus as a function of time for data Set 3. The rate is shown in units of mg per day, where time is indicated in days starting from the beginning of the run.

Chapter 5

Calibration, errors, and measurement precision

5.1 Electric field and drop radius

Rewrite Eq. (2.1) in the form

$$v_x = \left(\frac{Q}{6\pi\eta}\right)\left(\frac{E}{r}\right) \tag{5.1}$$

Consider non-fractional values of $Q = ne$, $n = 0, \pm 1, \pm 2, \ldots$. Then, as shown in Sec. 6.2, the measured values of v_x sharply peak at $n = 0, \pm 1, \pm 2, \ldots$. From a fit to the center of these peaks, Eq. (5.1) gives the fitted E/r ratio.

The electric field strength, E, is calculated from the measured voltage across the electric field plates, known to 3%, and the plate separation, 8.25±0.01 mm. The plates are parallel to within 0.1 mrad. Inserting the calculated value of E into the fitted E/r ratio, we obtain the drop radius r.

We have two additional checks of the drop radius, one from the measurement of the error caused by the Brownian motion, Sec. 5.2, and the other from the measurement of the net downward velocity of the drops, v_z in Eq. (2.3).

The drop radius depends to a moderate extent upon the size and shape of the voltage pulse applied to the drop generator and to a slight extent upon the age and

history of the drop generator. However over periods of hours the average drop radius could be taken to be constant, with fluctuations of $\pm 0.2\%$ for individual drops. Since the data were analyzed in one-hour-long blocks, the average E/r ratio for any given block was known to much better accuracy than this.

5.2 Brownian motion and drop position measurement errors

The precision of the determination of the drop charge depends upon the precision of the measurement of v_x. Consider the sequence of position measurements x_i of the trajectory of a drop. For two consecutive frames, j and $j-1$, the velocity measurement $v_{x,j}$ is given by

$$v_{x,j} \equiv \frac{x_j - x_{j-1}}{\Delta t}. \tag{5.2}$$

Here, Δt is the time between successive frames, 0.1 s in our case. Since Δt is known with very good precision, the error in measuring v_x comes from the error in determining the x_i of the drop centers, and from Brownian motion. Take the error in centroiding to be normally distributed with a standard deviation of σ_c.

During the time Δt between any two successive measurements of the x_i positions, Brownian motion adds a random contribution with standard deviation given by

$$\sigma_b = \sqrt{\frac{kT\Delta t}{3\pi\eta r}}. \tag{5.3}$$

Here k is the Boltzmann constant, T is the absolute temperature, η is the viscosity of air and r is the drop radius.

The trajectory of uncharged drops, which have no contribution to their trajectories due to the electric field, can thus be written as

$$\begin{aligned} x_j &= x_0 + \sigma_{c,j} + \sum_{i=2}^{j} \sigma_{b,i} \\ j &= 1, 2, \ldots, N_{images} \end{aligned} \tag{5.4}$$

with x_0 set by the initial position of the drop, and where the $\sigma_{c,i}$ ($\sigma_{b,i}$) are normally distributed with a std. dev. of σ_c (σ_b). The analysis for charged drops is similar if the effect of the electric field is first subtracted from the observed data points. It then follows that

$$v_{x,j}\Delta t = \sigma_{b,j} + \sigma_{c,j} - \sigma_{c,j-1} \tag{5.5}$$

and

$$\langle v_{x,j} v_{x,k} \rangle \, \Delta t^2 = \begin{cases} 2\sigma_c^2 + \sigma_b^2, & j = k \\ -\sigma_c^2, & |j-k| = 1 \\ 0, & \text{otherwise.} \end{cases} \tag{5.6}$$

Therefore the total error on any given velocity measurement, σ_v, is given by $\sigma_v^2 = 2\sigma_c^2 + \sigma_b^2$, and the centroiding error introduces an anti-correlation with magnitude $-\sigma_c^2$ in two consecutive velocity measurements, due to the shared position measurement. We use the concept summarized in Eq. (5.6) and the observed distributions of the $v_{x,i}$ (after removal of the contribution due to the alternating electric field) to separate σ_c from σ_b.

We find that averaged over this experiment

$$\sigma_c = 0.31 \ \mu\text{m}, \ \sigma_b = 0.47 \ \mu\text{m}, \tag{5.7}$$

in the measurement region. Compared to the size of an individual pixel on the CCD, the centroiding error is small, approximately 1/30 of a pixel. The value of σ_b obtained provides an independent check on the size of the drops, and is consistent with the size determined from the terminal velocity and the electric field drift velocity.

Equation 5.7 shows that the Brownian motion error, σ_b, is about the same magnitude as the error involved in finding the drop position, σ_c. Therefore substantially reducing σ_c through the use of smaller pixels will not by itself substantially reduce the error on the charge measurement, since the Brownian motion error can only be reduced by increasing N_{images}.

The final charge measurement of a drop is made using a single, detailed best fit to the entire observed trajectory of the drop, and the final error on the charge measurement σ_q is a result of propagating the errors σ_c and σ_b through this calculation.

5.3 Other sources of errors

We looked for other sources of errors, but all are negligible compared to those in Eq. (5.6). When we developed the upward air flow method we thought about the possibility that there might be some horizontal air velocity, $v_{x,air}$ in the measurement chamber, contributing an error to σ_v of order $v_{x,air} \times \Delta t$. By studying a large amount of data we found that the distribution of $v_{x,air} \times \Delta t$ had an rms value of 100 nm, and was a fixed property of the measurement region. For comparison $v_e \times \Delta t$ was of the order of 8 μm. These irregularities in $v_{x,air}$ are probably due to residual surface imperfections in the electric field plates. Since the irregularities are constant over long periods of time, they can be accurately measured and corrected for. For this analysis, that was not necessary.

Another possible source of error would be a non-uniformity in the electric field in the measurement region giving a horizontal gradient, dE/dx. This would produce a horizontal force on the drop's induced electric dipole moment. This dipole force acts in addition to the QE force. We found such a dipole force to be negligible compared to the QE force.

A small, vertical deceleration of the drops as they fall through the measurement chamber was observed. This amounted to a change of 30 μm/s in the apparent terminal velocity of the drops as they fell through the measurement region, or a systematic uncertainty in the radius of the drop of the order of 0.3%. We believe that the deceleration is due to the evaporation of the drop as it falls. The magnitude of this effect is small enough such that it can be neglected in the calculation of v_x. As a side note, any systematic uncertainties in the radius of the drops are absorbed by the calibration process described in Sec. 5.1, and do not affect the final charge measurement.

Similarly, other possible sources of measurement error such as apparatus vibrations, optical distortions and CCD array distortions, and patch non-uniformities on the electric field plates, were negligible.

Chapter 6

Data analysis and results

6.1 Drop selection criteria

In this section we use $q = Q/e$, a measure of the drop charge in units of the electron charge. We required that all drops used in the analysis meet the criteria in Table 6.1. The criteria are designed to maintain a charge measurement accuracy of approximately 0.03 e and to reject irregular drops caused by inconsistent operation of the drop generator.

6.1.1 $q < 9.5$ criterion

For any given drop there is an uncertainty in the radius of approximately 0.2% which contributes to the relative error on q. The *absolute* error on q thus increases linearly with q. Since the absolute error on q must be kept to the order of 0.03 e, restricting the data sample to drops with $q < 9.5$ keeps this contribution to less than 0.02 e. The overall charge distribution is such that only a few percent of the drops have q values outside this range.

6.1.2 $\sigma_q < 0.03$ criterion

Primarily, this criterion is a measure of N_{images} of the drop. Brownian motion and centroiding accuracy, characterized by σ_c and σ_b as described in Sec. 5.2, limit the

accuracy of the charge measurement, σ_q. For any given drop, the number of position measurements, N_{images}, and the state of the electric field during those measurements, in addition to σ_b and σ_c, determines this accuracy. As noted earlier, N_{images} was of the order of 15. If a drop has an exceptionally large radius or is falling too far from the centerline of the airflow tube, v_z will be too large and N_{images} will be too small.

6.1.3 χ^2 criterion

As mentioned earlier, the final calculation of the charge on a drop is done using a fit to the trajectory of the drop. It was required that the χ^2 probability of the fit to the drop's trajectory be better than 10^{-3}. This rejects a large class of rare artifacts based on the statistical likelihood that the observed deviations from the fitted trajectory could be attributed to the Brownian motion and centroiding errors. For example, a drop would be rejected if it had an anomalous trajectory due to vibrations in the apparatus or due to its charge having been changed by collision with an ion during measurement.

6.1.4 v_z criterion

The net downward velocity of the drop, v_z, depends upon the drop radius and the upward air velocity, v_{air}, Eq. (2.3). This criterion insures consistent drop radii within the hour long data blocks by requiring

$$|v_{z,drop} - v_{z,block}| < 0.124 \text{ mm/s} \tag{6.1}$$

where v_z is the measured value for one drop and $v_{z,block}$ is the average value of v_z for all the drops in the one hour data block. Using Eqs. 2.2 and 2.3, taking v_{air} as fixed and using an average value for r of 10 μm, this eliminates any drops with r different from the nominal value by more than about $\pm 0.5\%$.

Recall that the air velocity is approximately parabolic and that close to the centerline it is given by

$$v_{air}(x) = v_{air,0}\left[1 - (x/x_w)^2\right] \tag{6.2}$$

where x is the distance along the x axis from the centerline of the airflow tube, $x_w = 4.15$ mm is the distance to the wall of the tube, and $v_{air,0}$ is the air velocity along the centerline. Therefore this criterion indirectly restricts how far the drop can be from the centerline.

6.1.5 x deviation criterion

This criterion

$$|x - x_{block}| < 0.19 \text{ mm} \tag{6.3}$$

provides a direct constraint on how far a drop may deviate from the centerline in the x direction. Here x_{block} is the average value of x for all the drops in the one hour data block. The purpose of this criterion is to eliminate drops that were produced irregularly. The 0.19 mm upper limit in Eq. (6.3) was determined by examining the distribution of x positions of drops produced during normal operation of the drop generation and setting the upper limit to eliminate the tails.

6.1.6 Minimum distance R between any two drops criterion

The drops interact with one another through their induced electric dipole moments and viscous coupling through the air. Consider two drops of radius r, drop 1 moving with a velocity v_x due to the force of the electric field on its charge, as shown in Figure 6.1. This motion will move the surrounding air. At the position of drop 2, the velocity of the air in the x direction, $V_{x,disturbedair}$, is given by

$$V_{x,disturbedair} = \frac{3}{4}\frac{v_x r}{R}(1 + \cos^2\theta). \tag{6.4}$$

Since drop 2 sits in this disturbed air, its v_x due to the force of the electric field on its charge will have superimposed upon it $V_{x,disturbedair}$. This will distort the charge measurement. Therefore $V_{x,disturbedair}$ must be kept small by keeping R, the distance between the drops, much larger than r, the radius of the drop. A large separation also serves to minimize the interaction between the induced electric dipole moments of the

Table 6.1: Drop selection criteria. The entries are the percent removed by each criterion separately. The bottom row gives the total percent of drops removed by all criteria. Since the same drop may be removed by several criteria, the total percent removed is *not* the sum of the percent removed by the individual criteria.

Criterion	Set 1	Set 2
q	0.4	0.7
σ_q	6.0	0.3
χ^2	4.7	2.4
v_z	4.6	1.2
x	9.4	5.1
R	12.5	3.8
Total	22.3	8.7

drops, which increases as the inverse fourth power of the separation. We require

$$R > 0.62 \text{ mm} \tag{6.5}$$

separation between any two drops, which limits these forces to a small fraction of QE.

6.1.7 Summary and magnitude of drop selection criteria

Table 6.1 gives the percent of drops removed by each criterion averaged over each of the two data sets. The total percent of drops removed is also given. Since the same drop may be removed by several criteria, the total percent removed is *not* the sum of the percent removed by the individual criteria.

6.2 Results

After the application of these criteria we had a final data sample of 1.7×10^7 drops of average diameter 20.6 μm. The total mass of the sample was 70.1 mg. Figure 6.2 shows the charge distribution in units of e. (The asymmetry of the charge distribution

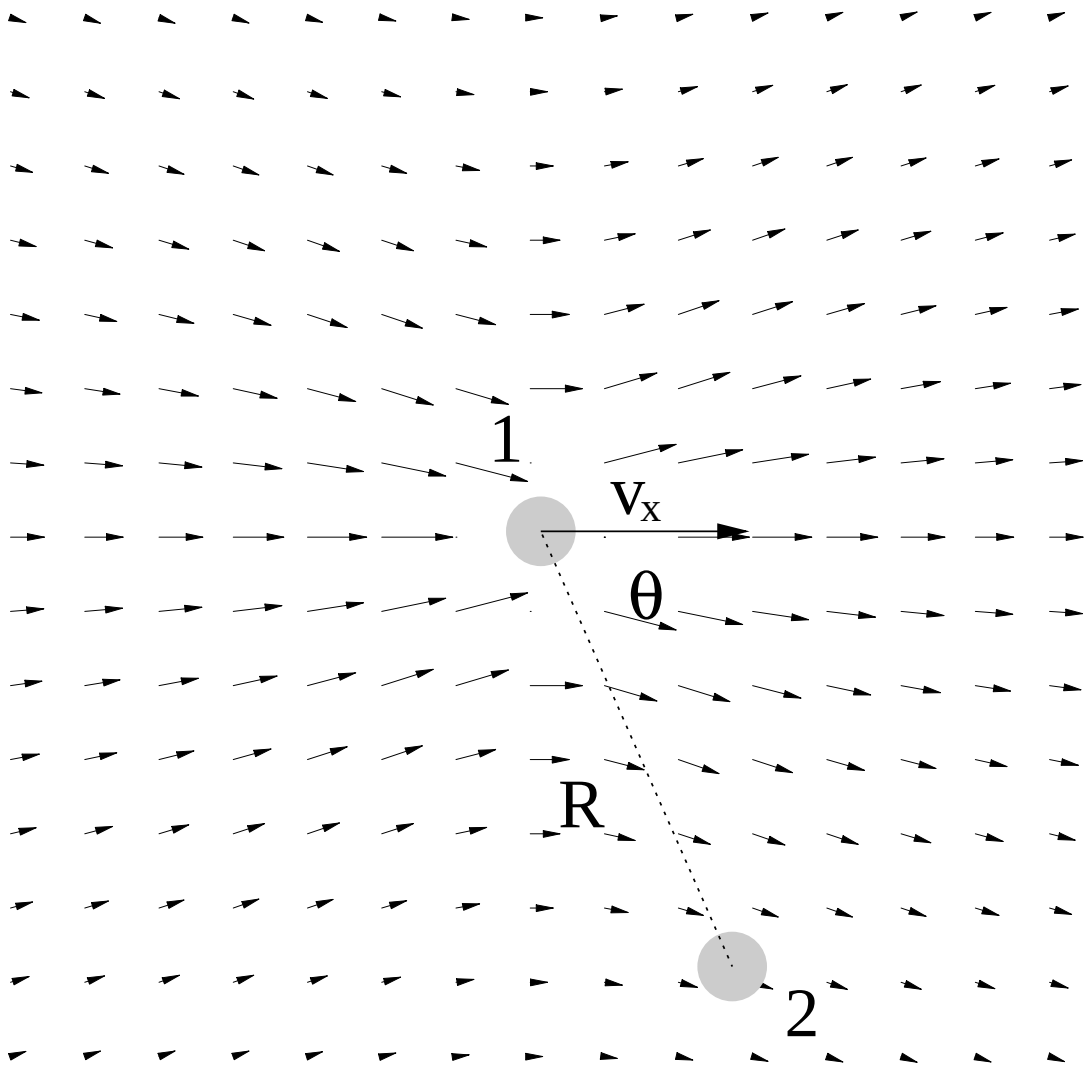

Figure 6.1: The viscous coupling between a moving drop 1 on a neighboring drop 2 in still air. The small arrows show the vector velocity of the disturbed air. Note that there is a slight disturbance at the position of drop 2 that will affect the trajectory of drop 2.

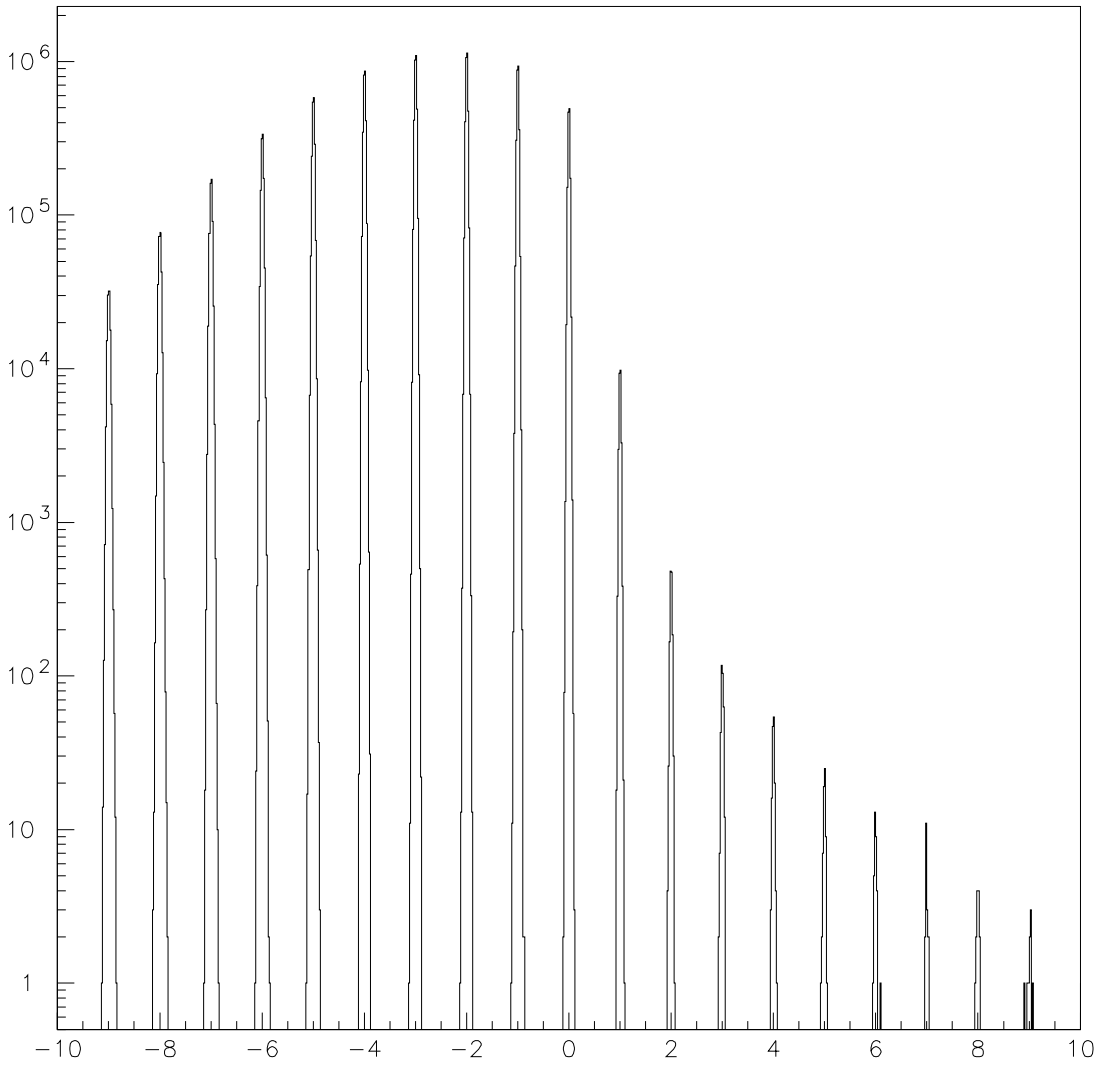

Figure 6.2: The q charge distribution in units of e.

is a property of the drop generator as discussed in Sec. 2.3.) We see sharp peaks at integer numbers of charges and no drops further than 0.15 e from the nearest integer. We emphasize that there is no background subtraction here, this is all the data after the application of the criteria previously discussed.

To show the shape of the peaks at integer values of q we superimpose them in Figure 6.3 using the charge distribution, q_c, defined by $q_c = q - N_c$ where N_c is the signed integer closest to q. The peaks have a Gaussian distribution with a standard deviation of 0.021 e. *The absence of non-Gaussian tails is what allows this search method to be so powerful.*

In Figure 6.4 we superimpose the valleys between the peaks using the residual charge distribution, q_r, defined by $q_r = q - N_l$ where N_l is the largest integer less than q. We did not find any drops with residual charge between 0.15 e and 0.85 e. In this residual charge range there are fewer than 1.17×10^{-22} fractional charge particles per nucleon in silicone oil with 95% confidence.

Thus this 70.1 mg search did not confirm the one unusual aspect of our previous 17 mg search, Halyo *et al.*[2], where we found 1 drop with a q_r of about 0.29 e. No such charge was found in this search. While it is of course still possible that the fractional charge found in the 17 mg experiment was real, we are inclined to believe that the 17 mg experiment had a very small background that has been eliminated by the improved method of this experiment.

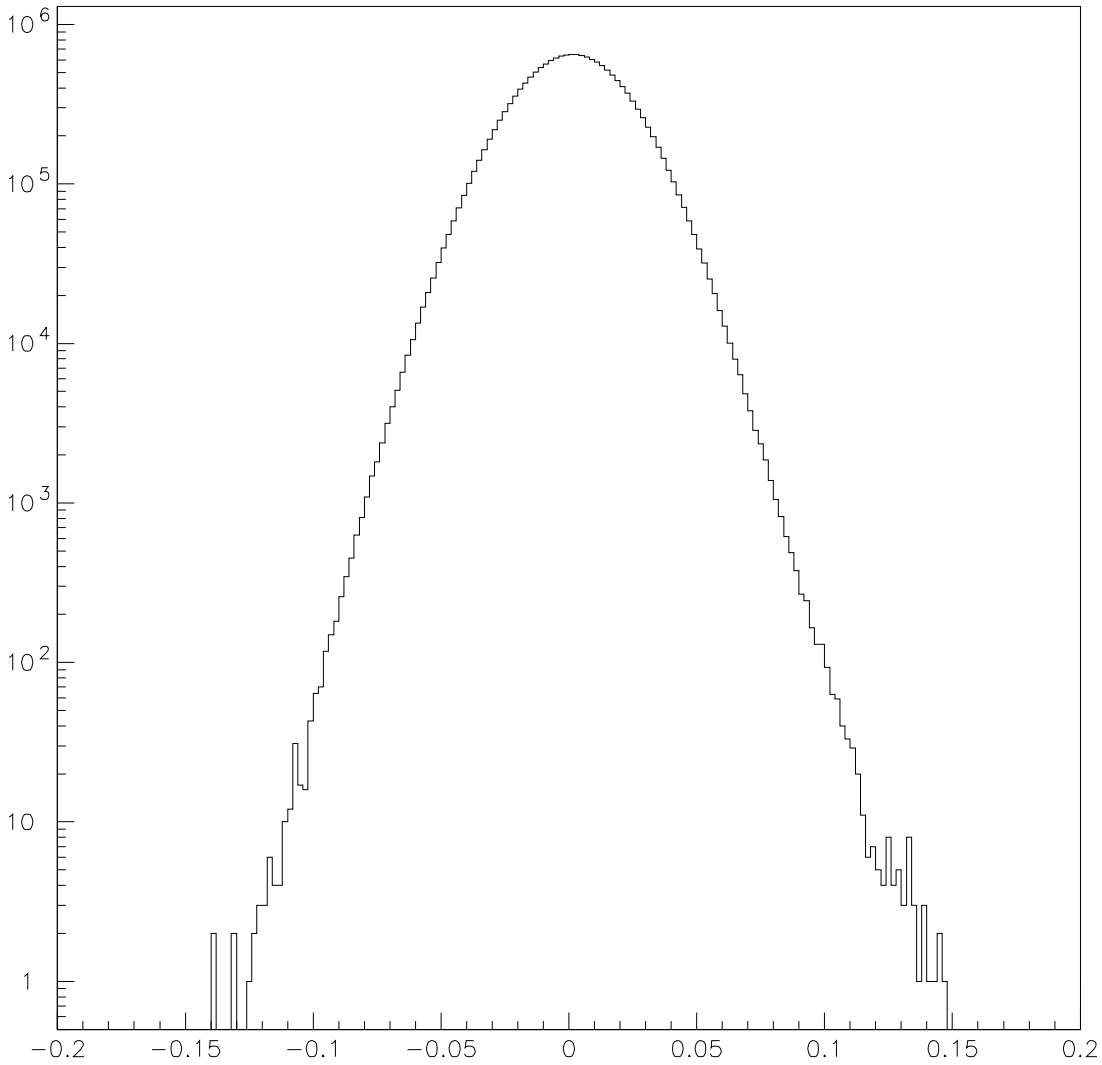

Figure 6.3: The q_c charge distribution in units of e.

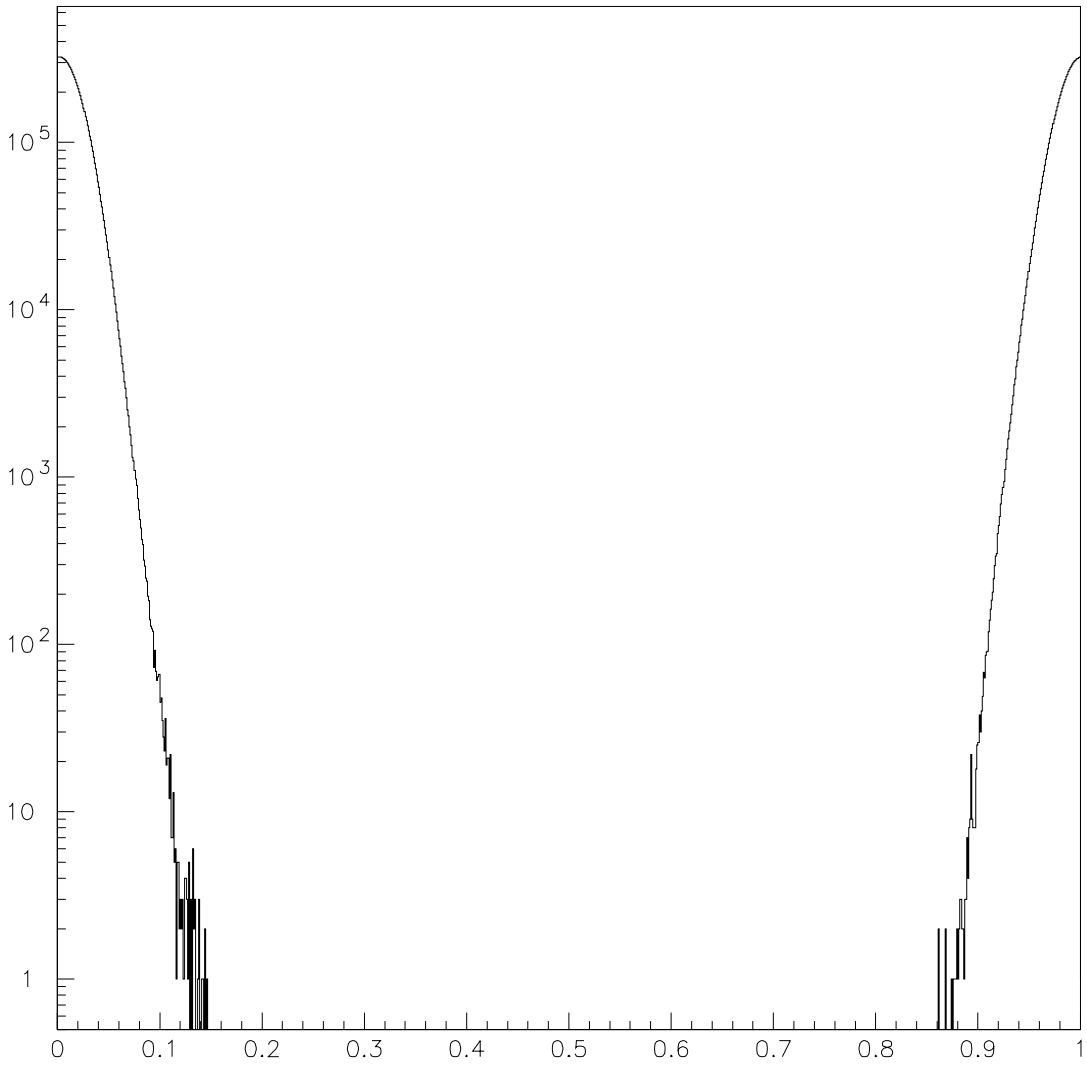

Figure 6.4: The q_c residual charge distribution in units of e.

Chapter 7

Conclusions

7.1 Comparison to other searches

In Table 7.1 we compare this search with previous, larger sample, searches for fractional charge particles in bulk matter. No evidence for fractional charge particles was found in the searches by Marinelli *et al.*[12], Smith *et al.*[15], and Jones *et al.*[4], similar to the null result in the present search.

In their super-conducting levitometer search in niobium, LaRue *et al.*[8] claimed to have fractional charge particles with $e/3$ and $2e/3$. But Smith *et al.*[15] who also searched in niobium using a ferromagnetic levitometer method did not find any such evidence in a four times larger sample. At present the results of LaRue *et al.*[8] are not understood and are generally not accepted.

Our search is by far the largest to date and has the smallest upper limit of any search on the concentration of fractional charge particles in bulk matter. But it is important not to generalize our limit to other kinds of bulk matter for several reasons. First, we do not know what happens to fractional charge particles that are in natural matter when that matter is processed. Note that except for the search in meteoritic material by Jones *et al.*[4], all the material in Table 7.1 is processed.

Second, if we assume the existence of stable, fractional charge particles, we do not know what natural materials are most likely to have a detectable concentration. Our

Table 7.1: Searches for fractional charge particles in ordinary matter. All experimenters reported null results except LaRue *et al.*[8]. There are 6.4×10^{20} nucleons in a milligram.

Method	Experiment	Material	Mass(mg)
levitometer	LaRue *et al.*[8]	niobium	1.1
levitometer	Marinelli *et al.*[12]	iron	3.7
levitometer	Smith *et al.*[15]	niobium	4.9
levitometer	Jones *et al.*[4]	meteorite	2.8
liquid drop	Halyo *et al.*[2]	silicone oil	17.4
liquid drop	this search	silicone oil	70.1

own thoughts are that the most promising natural material is that found in carbonaceous chondrite asteroids, since they are representative of the primordial composition of the solar system, having not undergone any geochemical or biochemical processes. Hence similar to the motivation of Jones *et al.*[4], our next search will be in meteoritic material from an asteroid.

7.2 Remarks on further use of this new method

The purpose of the new method [10] used in this experiment was to allow large drops to be used compared to the classical method, thus increasing the rate at which we could search through a sample and also enabling the use of suspensions of more interesting materials. We have succeeded in doing this, using drops of about 20 μm diameter compared to the approximately 10 μm diameter used in Halyo *et al.*[2]. In the Appendix we discuss further increasing the search rate by using still larger drops and by using multiple columns of drops to increase the total rate of drop production. We find that with this new method the mass per second search rate can be further increased by a factor of the order of 10, but probably not by a factor of a 100.

Appendix A

Optical Components

The lens, CCD camera, and light baffle were fixed to a rigid optical rail by means of adjustable slides which could be locked into a fixed position. Before the long data taking runs, there was a period of experimentation where these components were adjusted as the centroiding algorithm was being developed and tested.

Also, the lens itself was subjected to several tests to determine whether it was free of aberrations. By observing the image of a point source through the lens, it was possible to look for defects in the lens by examining the image for the particular defect of "coma", which appears as an elongation of the image of the point source, as the system is taken slightly out of focus. A wide aperture for the lens is desirable since it provides for less depth of field and sharper images, as well as requiring shorter illumination pulses. Unfortunately, in general aberrations increase as the aperture of a lens is increased (decreasing f-stop). The widest aperture (smallest f-stop) was used such that no coma was discernible over the entire field of view.

A low magnification is desirable since it maximizes the field of view, and thus the number of measurements which can be made on any given drop. However, when the magnification is too small, the positions of the drop images cannot be measured precisely. The optimal magnification setting was found by taking data with several different values. The lowest magnification in which centroiding accuracy was not significantly degraded was used.

After these experiments were complete, these components were all epoxied into

Figure A.1: Image of optical calibration target

place to prevent any accidental modification of the optical parameters. Since this fixes the positions of and distance between the lens and CCD (which defines the image plane), the object plane is also in a known position relative to the optical rail. Objects in this plane appear in focus. During data taking, the position of the optical rail was always adjusted to optimize the focus of the drops, thus ensuring that the drops are in the object plane, which implies consistent positioning of the optical rail.

A final, careful measurement of the magnification was done after data taking was complete. A precise optical calibration target was placed in the object plane, and its images (see Figure A.1) were recorded. This optical target was a grid, with a 0.5 mm spacing in both directions.

A program was written to carefully measure the positions of the horizontal and vertical lines to sub-pixel accuracy. This provided the precise calibration of the magnification of the optical system to better than 0.1%. In actuality, the exact magnification is not known since the size of the CCD is not known precisely. What *is* known is the conversion factor between pixels to real distances, which is in any case the relevant quantity. This conversion factor was determined separately for the x and z directions.

Appendix B

Airflow duct parameters

The design of the airflow duct was constrained by several factors coming from integrating laminar airflow with capacitor plates. The best possible charge resolution is achieved with the highest possible electric fields, but these fields must be made as uniform as possible. Larger capacitor plates provide a more uniform field, however, laminar air flow is more difficult to achieve in a larger duct. In addition, there is a general need to minimize as much as possible the size of the duct for convenience. The eventual design chosen was a rectangular duct consisting of two stiff G10 composite walls with embedded aluminum capacitor plates, precisely spaced by two lexan windows. The cross section of the duct is shown in Figure B.1.

B.1 Electric field plates

The maximum voltage with which we were able to work was in the neighborhood of ± 15 kV. This is a result of the design of the electric field switcher, which was a single-tube pulldown design based on the 6BK4B. The voltage rating on the 6BK4B is 25 kV, but with individual testing of tubes it was possible to find units capable of supporting up to 36 kV (± 18 kV) of potential difference. The maximum voltage available effectively sets the plate spacing, since arcing caused by breakdown of the air occurs at field strengths of 3 MV/m under ideal conditions. Because of the inevitable electric field concentrations and surface contamination, it was only possible to achieve

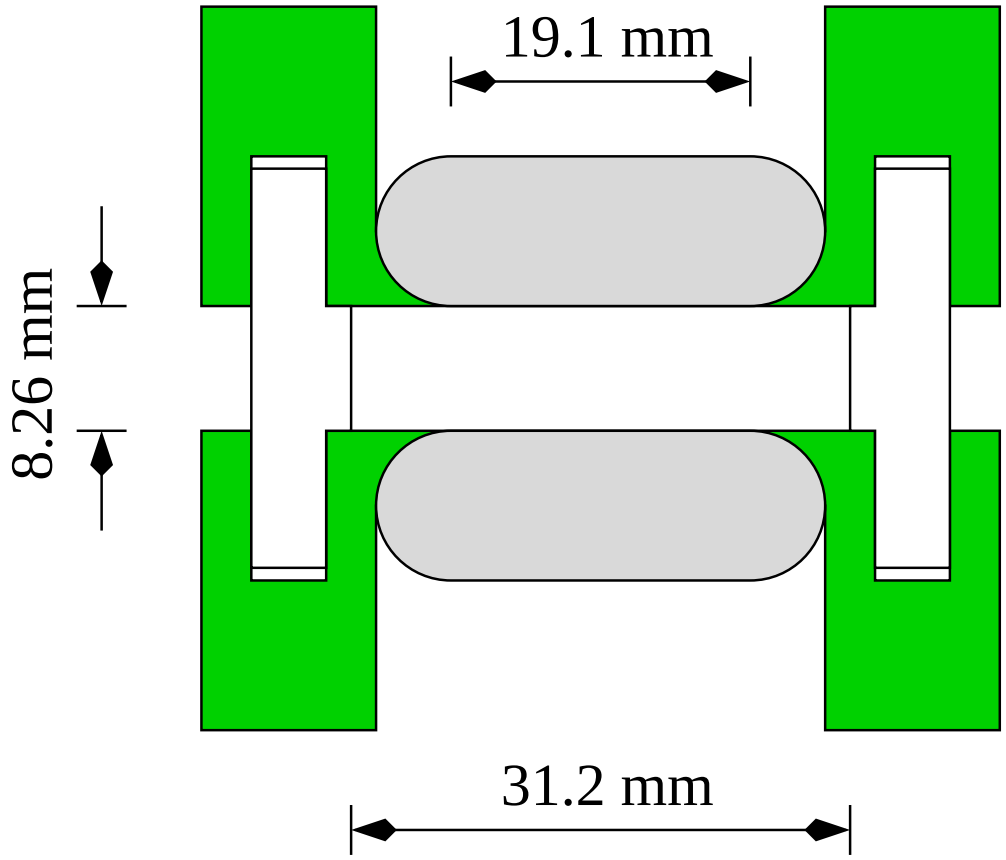

Figure B.1: Cross sectional diagram of the airflow duct, with embedded capacitor plates and transparent lexan windows for viewing the measurement region.

~ 2 MV/m field strengths in practice. This resulted in the plate spacing being set at 8.255 mm, at 15 kV potential difference.

The effect of the fringing fields of a finite parallel plate capacitor decrease proportionally to $e^{-\pi\frac{\rho}{d}}$ in the region near the edge of the plates, where d is the spacing between the plates, and ρ is the distance inwards from the edge. By choosing the long axis of the plates to be 25.4 mm in both directions from the measurement region, the fringe field effects at least from the short edges of the plates can be made negligible, on the order of 10^{-4}. The effects of the long edges are significant, however, since they are only ~ 1 plate separation from the measurement region, and are only attenuated by a factor of $\sim 10^{-2}$. A mitigating effect is the material (G10 composite) making up the wall of the duct, which tends to prevent the electric field from diverging quite as quickly as the field from identical plates in air. In order to verify the quality of the electric field, a realistic numerical simulation of the duct cross section was done using the standard Poisson/Superfish package courtesy of Los Alamos National Lab. Since the target charge measurement accuracy is on the order of 3%, the minimum plate size was found such that the variations in the QE force encountered by the drops would be much less than this. The results of the simulation, drawn in Figure B.2 and Figure B.3, clearly show the walls tending to confine the field within the channel, effectively extending the plates slightly. In addition, it is clear in the magnified view that the exposed surface of the plates, especially near the discontinuity from the aluminum plate to the G10 composite wall, is free of efield concentrations.

The systematic electric field variations in the small measurement region centered in the middle of the duct are calculated to be less than 10^{-3}, as shown in Figure B.4 and Figure B.5.

The result was surprising in that an unexpectedly small plate width of 19.1 mm was satisfactory, and was eventually used. Incidentally, the asymmetry in the E_x field moving across the duct in the x direction is due to the fact that only one plate is driven with high voltage, while the other plate is fixed at ground potential. Since the remainder of the apparatus, particularly the metal support structures are also fixed at ground potential, there is an inherent asymmetry. This was simulated by requiring that the potentials all fall to zero at a realistically placed rectangular boundary.

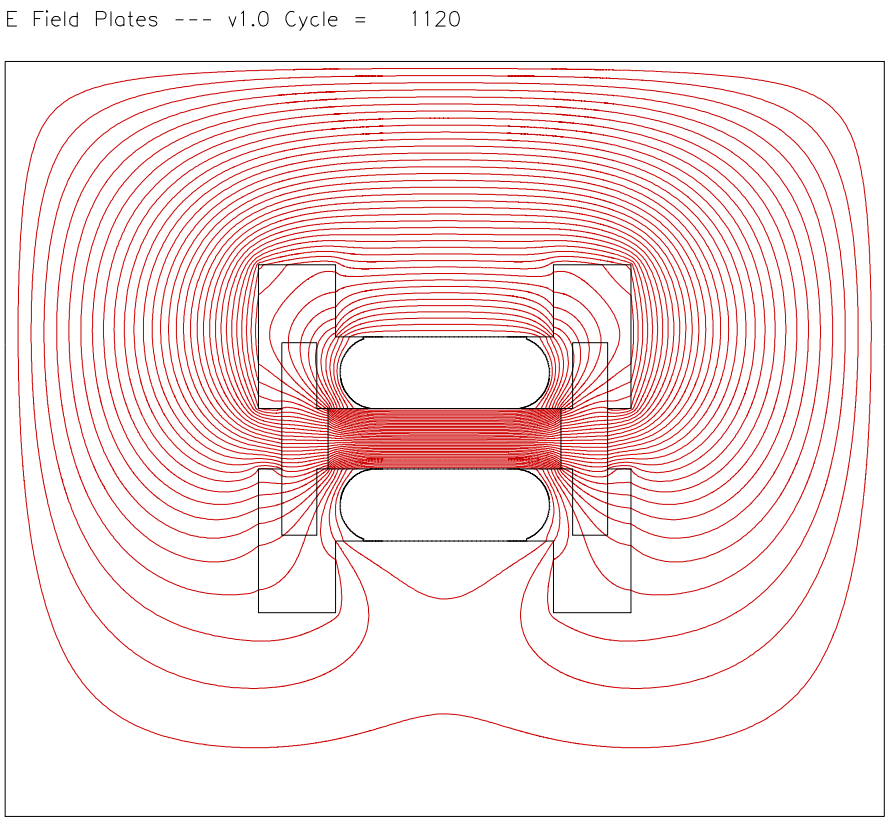

Figure B.2: Equipotential lines from a detailed, realistic numerical simulation of the combined airflow duct and capacitor plates.

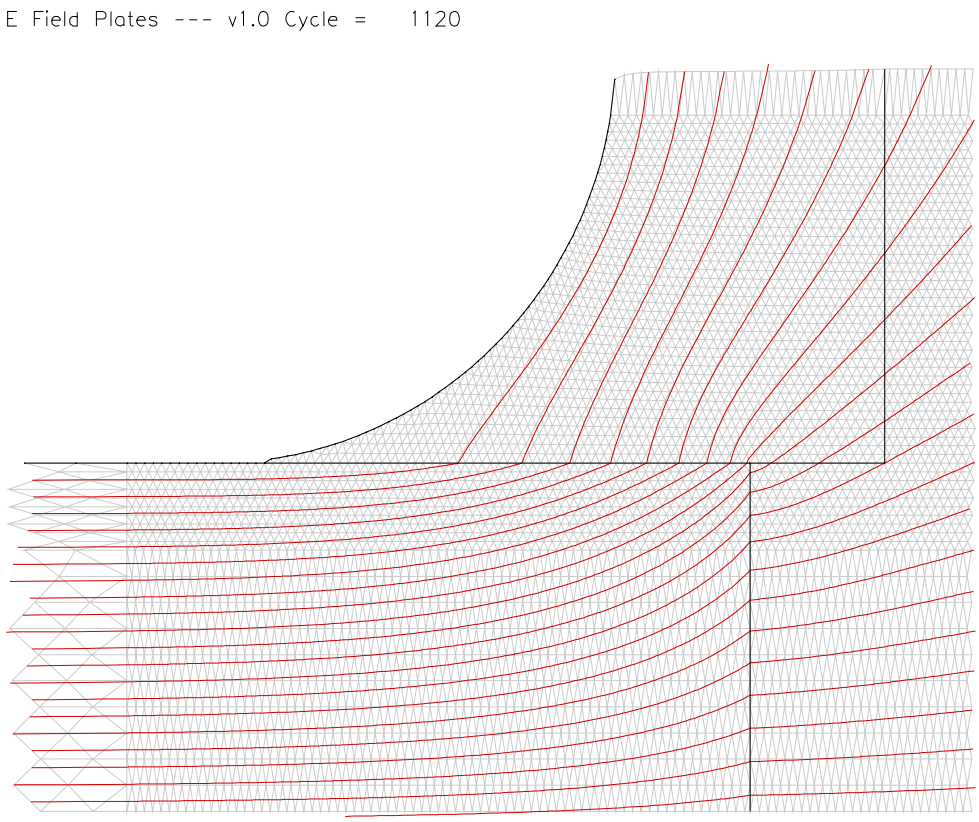

Figure B.3: Equipotential lines near the discontinuity where the aluminum and G10 composite components meet.

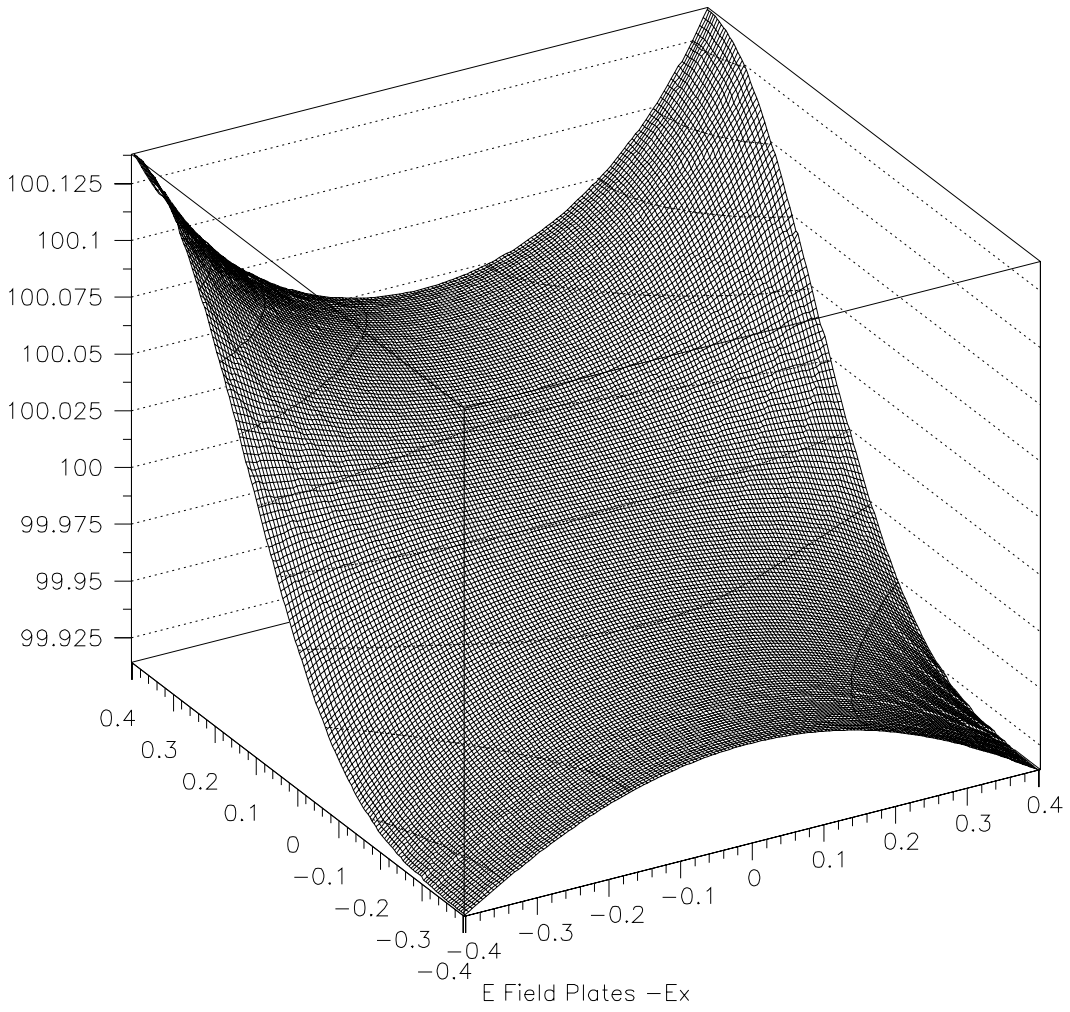

Figure B.4: The behavior of E_x in a 4 mm by 4 mm region in the x-y plane centered on the measurement region. All values are normalized to the nominal value of 100 directly in the center of the chamber. The left to right axis is the y direction, while the front to back axis is the x direction, from the grounded capacitor plate to the high voltage plate.

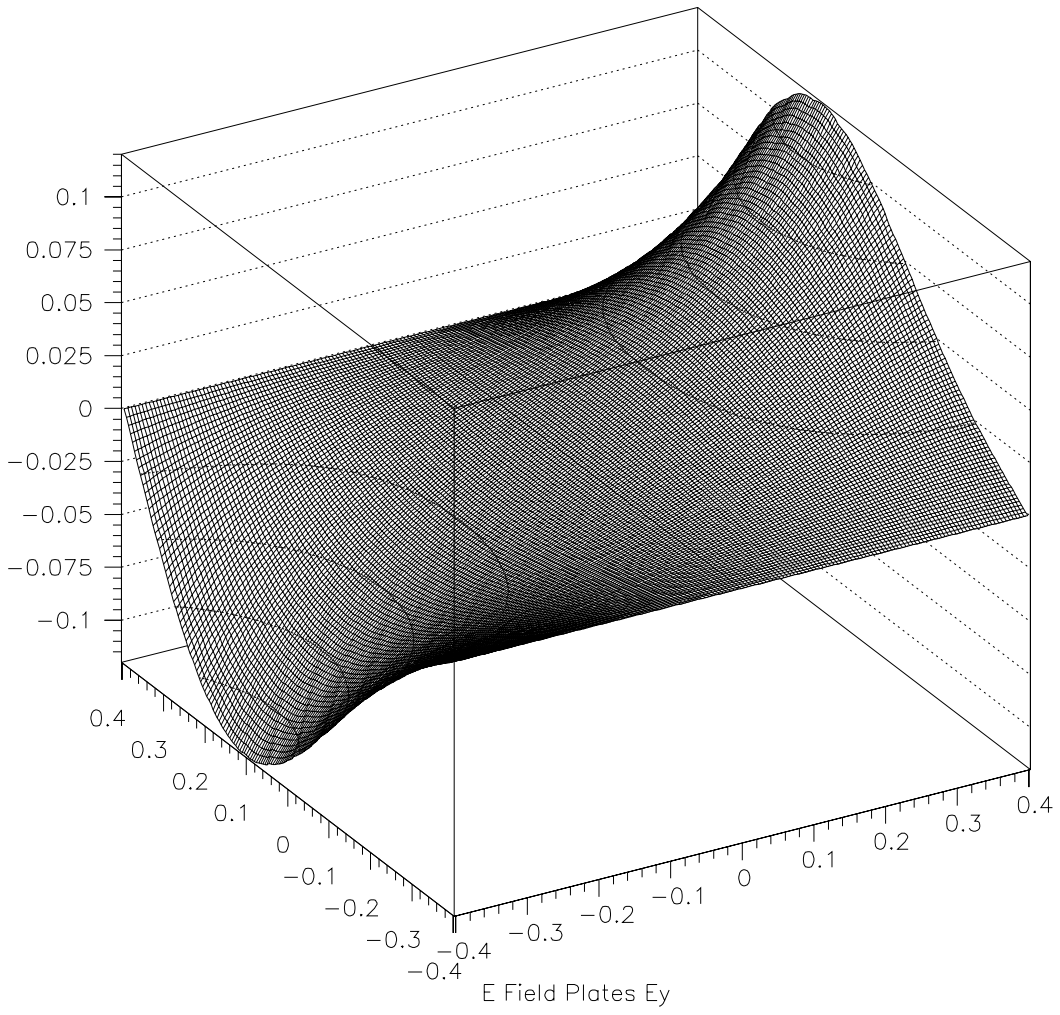

Figure B.5: The behavior of E_y in a 4 mm by 4 mm region in the x-y plane centered on the measurement region. All values are normalized to the nominal value of 100 directly in the center of the chamber. The left to right axis is the y direction, while the front to back axis is the x direction, from the grounded capacitor plate to the high voltage plate.

Since dipole effects in general will draw the drop towards regions of higher field, the energized field plate will always be slightly attractive.

It turns out that the dipole interaction between the induced dipole moment of the drop and any electric field inhomogeneities $\nabla(\vec{\rho}\cdot\vec{E})$ is larger in magnitude than the variation in the QE force. The primary sources of electric field inhomogeneity are the fringe field effects, any non-parallelism between the two plates, surface imperfections in the plates, and the "patch effect", or variations in the surface potential of the plates due to contaminants, which were all estimated to be small. This was eventually verified after analysis, see Sec. 5.3, which showed that the total contribution due to these and other effects is on the order of 1% of the QE force on a single charge.

B.2 Airflow duct

The cross sectional dimensions of the duct are based on the 19.1 mm width of the electric field plates, and the maximum possible plate separation, 8.26 mm as mentioned above. For reasonably clean surfaces, surface tracking of high voltage can cause arcing between the plates at field strengths a factor of ~ 2.5 below breakdown levels. For this reason, the lexan windows are spaced at a distance such that the shortest path along any surface from one plate to the other is ~ 2.5 times the spacing between the plates, yielding a duct 31.2 mm long in the y direction.

For slow viscous flow through a rectangular duct, once the flow reaches steady state, the flow profile across the cross section is found by solving Poisson's equation with the appropriate boundary conditions (zero velocity at the walls of the duct). This has been solved exactly, as described in [7], and the solution is given by

$$u(x,y) = 1 - \frac{x^2}{b^2} + \frac{32}{\pi^3}\sum_{n=1,3,5}^{\infty}\frac{(-1)^{2n-1}}{n^3}\frac{\cosh\left(\frac{n\pi y}{2b}\right)\cos\left(\frac{n\pi x}{2b}\right)}{\cosh\left(\frac{n\pi a}{2b}\right)} \tag{B.1}$$

.

In Eq. (B.1), the velocity (normalized to the maximum flow velocity found in the center of the duct) $u(x,y)$ is given in terms of the position in the duct given by x and y, and the half widths of the duct a and b, which are in the long and short directions

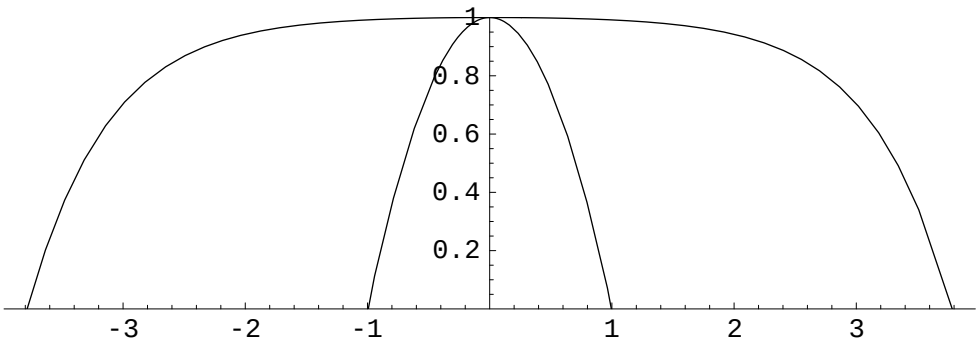

Figure B.6: The normalized flow velocity profiles across the axes of symmetry of a rectangular duct. The approximately parabolic profile is taken across the short axis.

respectively. This normalized flow velocity is plotted across the center of the long and short axes of the duct in Figure B.6.

This steady state flow is well understood and confirmed by direct measurement using terminal velocity measurements of drops. In the measurement region, the variation in the y direction is negligible, since along the long axis of the duct, there is a large region where the flow is essentially uniform. Across the short axis, where the flow is approximately parabolic, there is an approximately 1 mm wide region where the flow is uniform to $\sim$ 1%. Since the flow is adjusted such that the drops fall at 1/10 their normal terminal velocity, the final variation in drop velocities in the measurement region is on the order of $\sim$ 10%.

The length of the duct was required to be such that the non-equilibrium flow from the inlet at the bottom of the duct, which is a simple union to 1/4 inch copper tubing, has time to develop into the steady state profile described above. The required inlet length is empirically found [1] to be

$$0.06(Re)(a) \tag{B.2}$$

where a is the width of the duct (the width of the long axis is used, since that gives an upper bound) and Re is the Reynolds number, given by

$$Re \equiv \frac{\rho a v}{\eta} \tag{B.3}$$

where a is the characteristic length of the system (again, the width of the long axis of the duct is used for an upper limit), ρ is the fluid (air) density, v is the flow velocity, and η is the fluid (air) viscosity. For the flow velocities used in this experiment, the Reynolds number for the flow in the duct is well below 100. These low Reynolds numbers are also useful to demonstrate that the flow is, in fact, laminar. Empirical studies show that laminar flow is possible up to Reynolds numbers on the order of 2×10^3 [1]. The duct was designed to allow for flows up to 3 cm/s, requiring an inlet length of ~ 20 cm. Eventually, the duct was made 30.5 cm long, with 20 cm of inlet below the measurement region. The remaining length of duct above the capacitor plates was left to ensure that having the outlet of the duct open to the air would have a negligible effect on the flow at the measurement region.

Appendix C

The trajectory of a drop

If Brownian motion is for the moment ignored, and in the approximation where the time constant for the drop to reach terminal velocity is negligible, the trajectory of a drop in the measurement region with charge q and terminal velocity $v_{z,term}$ can be written as

$$\begin{aligned} x(t) &= x_0 + v_{x,tilt}t + \left(\frac{q}{6\pi\eta r}\right)\int_{t'=0}^{t'=t} E(t')dt' \\ y(t) &= y_0 + v_{y,tilt}t \\ z(t) &= z_0 + (v_{z,term} - v_{air})\,t \end{aligned} \tag{C.1}$$

.

The constant terms $v_{x,tilt}$ and $v_{y,tilt}$ are necessary to handle any small misalignment from vertical both of the camera and of the airflow tube, as well as possible dipole effects due to electric field inhomogeneities (see Sec. B.1). The electric field $E(t)$ is taken to be spatially uniform, with a periodic variation in time, due to the alternating high voltage applied to the capacitor plate. If we define for convenience an arbitrary constant, nominal electric field value $E_{nominal}$, the x component of the trajectory can be written as

$$x(t) = x_0 + v_{x,tilt}t + v_{e,nominal}\int_{t'=0}^{t'=t} \frac{E(t')}{E_{nominal}}dt' \tag{C.2}$$

.

Since the position of the drop is only measured periodically in time with interval Δt, it is only necessary to calculate the series of position values x_i, y_i and z_i for $i \in 1, 2, 3 \ldots$. Also, since the electric field has a period of precisely $4\Delta t$, the expression in the integrand can be simplified by defining the series of constants p_i according to

$$\begin{aligned} p_0 &= \frac{1}{\Delta t E_{nomimal}} \int_{t'=3\Delta t}^{t'=4\Delta t} E(t')dt' \\ p_1 &= \frac{1}{\Delta t E_{nomimal}} \int_{t'=0}^{t'=\Delta t} E(t')dt' \\ p_2 &= \frac{1}{\Delta t E_{nomimal}} \int_{t'=\Delta t}^{t'=2\Delta t} E(t')dt' \\ p_3 &= \frac{1}{\Delta t E_{nomimal}} \int_{t'=2\Delta t}^{t'=3\Delta t} E(t')dt' \\ p_n &= p_{n-4} \end{aligned} \tag{C.3}$$

.

By working in units where Δt is 1, and by a good choice of $E_{nominal}$, it can be arranged so that the "polarities" p_i have magnitude ~ 1, with signs alternating in the pattern $\ldots, +, +, -, -, +, +, -, -, \ldots$, reflecting the fact that two measurements are always taken between the alternations of the direction of the electric field.

The trajectory is then concisely written as

$$\begin{aligned} x_i &= x_0 + v_{x,tilt} i + v_{e,nominal} \sum_{j=1}^{i} p_i \\ y_i &= y_0 + v_{y,tilt} i \\ z_i &= z_0 + \left(v_{z,term} - v_{air}\right) i \end{aligned} \tag{C.4}$$

.

It is now a simple matter to include the effects of Brownian motion. Brownian motion contributes one step of a random walk between every pair of measurements, where each step is a random deviate drawn from a Gaussian with a standard deviation

given by Eq. (5.3). The Brownian motion of a drop is then described by a sequence of numbers $\sigma_{b,i}, i = 1, 2, 3, \ldots, N_{images}$, for each axis. At any time, the total deviation from the idealized trajectory described above is the *s*um of all of the previous steps—this is the nature of a random walk.

Finally, the measured trajectory differs from the actual trajectory due to the centroiding process. These errors contribute random measurement errors to the position of each point, which are assumed to be Gaussian distributed with standard deviation. Each drop then has an associated sequence of centroiding error values $\sigma_{c,i}, i = 1, 2, 3, \ldots, N_{images}$ for each axis. The CCD is not symmetric in x and z since the pixels are not square. For this reason, the sequences $\sigma_{c,x,i}$ and $\sigma_{c,z,i}$ are drawn from distributions with different standard deviations, which were determined from the data by the procedure described in Sec. 5.2. In this experiment, there was no attempt to measure the y positions of the drops, although it is conceivable to do so by quantifying the focus information contained in each drop image. Hypothetically, the errors in this process would contribute similarly.

The final measured trajectory is given by

$$\begin{aligned} x_i &= x_0 + v_{x,tilt} i + v_{e,nominal} \sum_{j=1}^{i} p_i + \sum_{j=1}^{i} \sigma_{b,x,i} + \sigma_{c,x,i} \\ y_i &= y_0 + v_{y,tilt} i + \sum_{j=1}^{i} \sigma_{b,y,i} + \sigma_{c,y,i} \\ z_i &= z_0 + \left(v_{z,term} - v_{air}\right) i + \sum_{j=1}^{i} \sigma_{b,z,i} + \sigma_{c,z,i} \end{aligned} \tag{C.5}$$

.

Appendix D

Trajectory fitting calculation

Least squares fitting is well understood and is described in detail in [13]. A typical fitting problem involves n data points $y_i, i = 1, 2, 3, \ldots, n$ each of which is known with some uncertainty $\sigma_i, i = 1, 2, 3, \ldots, n$, and finding the function f of the independent parameter i such that the n fitted values $Y_i \equiv f(i), i = 1, 2, 3, \ldots, n$ best approximate the y_i data points. The functional form of f is specified and can only be varied through m adjustable parameters $a_i, i = 1, 2, 3, \ldots, m$, so that $f \equiv f(a_1, a_2, a_3, \ldots, a_m, i)$.

The "best approximate" f is specified by the set of a_i values such that the χ^2 is minimized.

$$\chi^2 \equiv \sum_{i=1}^{n} \left(\frac{Y_i - y_i}{\sigma_i} \right)^2 \tag{D.1}$$

When f is *l*inear in the parameters a_i, it is possible to write $f(a_1, a_2, a_3, \ldots, a_m, i)$ as a sum of basis functions $g_1(i), g_2(i), g_3(i), \ldots, g_m(i)$

$$f(a_1, a_2, a_3, \ldots, a_m, i) = a_1 g_1(i) + a_2 g_2(i) + a_3 g_3(i) + \ldots a_m g_m(i) \tag{D.2}$$

The well known result involves defining the *d*esign matrix $\mathcal{A}$ and the vector b_i.

$$\mathcal{A}_{ij} = \frac{g_j(i)}{\sigma_i} \tag{D.3}$$

$$b_i = \frac{y_i}{\sigma_i}$$

The general solution for the best fit a_i values is then given (in matrix form) by

$$\left(\mathcal{A}^T \cdot \mathcal{A}\right)^{-1} \cdot \mathcal{A}^T \cdot \mathbf{b} \tag{D.4}$$

where the T superscript denotes the matrix transpose.

This solution is correct for the case where the data points are statistically independent, as reflected in the fact that the errors associated with the data points are given by a vector σ_i, which are essentially the diagonal elements of the full error matrix σ_{ij}. As described in Sec. 5.2, the data points in a drop trajectory are *n*ot independent, due to the statistics of Brownian motion. Furthermore, since the two sources of statistical uncertainty, centroiding error and Brownian motion are of comparable magnitude, it is not possible to simplify the fitting problem simply by fitting the differences between adjacent points. Specifically, we have a trajectory of the form

$$x_i = f_i + \sum_{j=1}^{i} \sigma_{b,i} + \sigma_{c,i} \tag{D.5}$$

where f corresponds to the trajectory in the absence of Brownian motion or centroiding error, and the $\sigma_{b,i}$ and $\sigma_{c,i}$ are a sequence of random deviates representing those sources of error, as described in Sec. 5.2. Clearly, $\langle x_i x_{i-1} \rangle$ is not zero due to the Brownian motion terms.

The differences between adjacent points are given by

$$\Delta x_i \equiv x_i - x_{i-1} = f_i - f_{i-1} + \sigma_{b,i} + \sigma_{c,i} - \sigma_{c,i-1} \tag{D.6}$$

.

In centroiding error were negligible, then $\langle \Delta x_i \Delta x_{i-1} \rangle$ would be zero, and it would be possible to fit the sequence of Δx_i to the new function $f_i' \equiv f_i - f_{i-1}$. Unfortunately, this is not the case. In fact, this was attempted during early stages of the analysis, and found to be unsatisfactory.

It turns out to be fairly easy to generalize linear fitting as described above to the

case where there are correlations. Begin by redefining the design matrix, removing the σ_i dependence:

$$\mathcal{A}_{ij} = g_j(i) \tag{D.7}$$

The vector of fitted values is then given by $\mathcal{A}\mathbf{a}$, and the vector of residuals by $\mathcal{A}\mathbf{a} - \mathbf{y}$. The χ^2 can then be written as

$$\chi^2 = (\mathcal{A}\mathbf{a} - \mathbf{y})^T \, \sigma^{-\mathbf{1}} \, (\mathcal{A}\mathbf{a} - \mathbf{y}) \tag{D.8}$$

.

It is then straightforwards to show that the minimization requirement on χ^2, $\frac{\partial}{\partial \mathbf{a}}\chi^2 = 0$ leads directly to

$$\mathbf{a} = \left(\mathcal{A}^T \sigma^{-\mathbf{1}} \mathcal{A}\right)^{-1} \mathcal{A}^T \sigma^{-\mathbf{1}} \mathbf{y} \tag{D.9}$$

,

which is precisely the required formula for the best fit a_i in terms of the data points y_i, and error matrix σ_{ij}. For a specific, relevant example, recall from Sec. C and Eq. (C.6) that the form of the drop trajectory is given by

$$x_i = x_0 + v_{x,tilt} i + v_{e,nominal} \sum_{j=1}^{i} p_i + \sum_{j=2}^{i} \sigma_{b,x,i} + \sigma_{c,x,i} \tag{D.10}$$

.

Data of this form is best described by the model

$$f_i = a_1 + a_2 i + a_3 \sum_{j=i}^{i} p_i \tag{D.11}$$

where the best fit a_1, a_2, and a_3 for any given set of data points correspond to the best estimate of x_0, $v_{x,tilt}$ and $v_{e,nominal}$ respectively. The basis functions $g_j(i)$ are then given by

$$g_1(i) = 1$$
$$g_2(i) = i \tag{D.12}$$
$$g_3(i) = \sum_{j=1}^{i} p_i \tag{D.13}$$

and the error matrix σ_{ij} is given by

$$\sigma_{ij} \equiv < x_i x_j > - < x_i >< x_j >= \begin{cases} \sigma_c^2 + i\sigma_b^2 & i < j \\ \sigma_c^2 + j\sigma_b^2 & \text{otherwise} \end{cases} \tag{D.14}$$

.

As a concrete example, in the case where there are 7 data points, $\sigma_b = \sigma_c = 1$, and the p_0, p_1, p_2, p_3 are given by -1, -1, 1, and 1 respectively, we have:

$$\mathcal{A} = \begin{matrix} 1 & 1 & -1 \\ 1 & 2 & -2 \\ 1 & 3 & -1 \\ 1 & 4 & 0 \\ 1 & 5 & -1 \\ 1 & 6 & -2 \\ 1 & 7 & -1 \end{matrix} \tag{D.15}$$

$$\sigma = \begin{matrix} 2 & 1 & 1 & 1 & 1 & 1 & 1 \\ 1 & 3 & 2 & 2 & 2 & 2 & 2 \\ 1 & 2 & 4 & 3 & 3 & 3 & 3 \\ 1 & 2 & 3 & 5 & 4 & 4 & 4 \\ 1 & 2 & 3 & 4 & 6 & 5 & 5 \\ 1 & 2 & 3 & 4 & 5 & 7 & 6 \\ 1 & 2 & 3 & 4 & 5 & 6 & 8 \end{matrix} \tag{D.16}$$

and

$$v_{e,nominal} \equiv a_3 = \frac{1}{9}x_1 - \frac{17}{54}x_2 + \frac{1}{54}x_3 + \frac{10}{27}x_4 + \frac{1}{54}x_5 - \frac{17}{54}x_6 + \frac{1}{9}x_7 \tag{D.17}$$

Appendix E

Pattern Recognition and Tracking

The initial stage of data processing converts the raw data— a series of sequential 8-bit greyscale images into drop trajectory data. To accomplish this, the images of the measurement region are first analyzed in order to recognize the individual drop images present, after which the positions of each drop image or centroid are precisely calculated. Since multiple drops appear in the measurement region simultaneously, a pattern recognition algorithm was used to identify which centroids form the trajectory of any given drop.

The image recognition aspect of this task is made simpler because of the controlled environment. The operating point for the background illumination was chosen to maximize the signal to noise ratio produced by the camera response function for the image of a typical drop. Since the contrast in the drop images increased with increased illumination, while the rms fluctuations in each pixel reached a limiting value of ≈ 1 greyscale units, signal to noise increased with increasing illumination. The illumination level was set at the maximum possible without operating any of the pixels of the camera in saturation. This background illumination was made as spatially uniform as possible, however there was inevitable variation due to vignetting caused by the restricted aperture provided by the airflow tube. This variation was approximately 28 greyscale units, or roughly 10%, with the image being brightest in the center. These background values were measured and recorded for each pixel once per hour at the beginning of each block of data.

A typical drop image had a contrast of ≈ 90 greyscale units. Each pixel of the CCD was read out as an 8-bit number, 0–255, with 255 being brightest and 0 being darkest. The drop images were dark, on a bright background. A simple thresholding operation comparing the value of each pixel with the corresponding background value was used to detect the presence of a drop image, and a recursive algorithm using an adjacency criteria grouped neighboring pixels together to form centroids. From this, a rough measurement of the position of the drop image was possible using a center of mass calculation. To achieve the required accuracy, it was necessary to minimize the effects of camera noise and variations in background illumination, as well as allow the tails of the drop image to enter into the position calculation. A second calculation, operating on a 13×21 region centered around the rough center of mass, measured the x (z) position by summing the pixels in the vertical (horizontal) direction and fitting the result to a Gaussian.

After each image has been converted to a list of centroid positions, the centroids from the same drop in different images must be associated together into a single trajectory. It is important that errors be avoided at this stage since a trajectory containing even a single incorrectly associated point will most likely appear to carry a fractional charge. In addition, for this experiment it was necessary to process on the order of 10^8 events with minimal tracking artifacts. Heuristic techniques were therefore completely avoided in favor of a brute force combinatorial technique. The algorithm used maintains an internal state consisting of a list of "known" drops for which some amount of data exists and the future trajectory is calculable, and a buffer of 5 images worth of past centroid data. The algorithm applies the following procedure to every incoming image:

1. The expected positions of all "known" drops are calculated. This calculation is based on a best fit to the known trajectory of the drop, using the propagated error from this fit to determine the region most likely to contain the new centroid. This is diagrammed in Figure E.1

2. The current image is checked for centroids in the expected positions. Several different cases are possible, as shown in Figure E.2

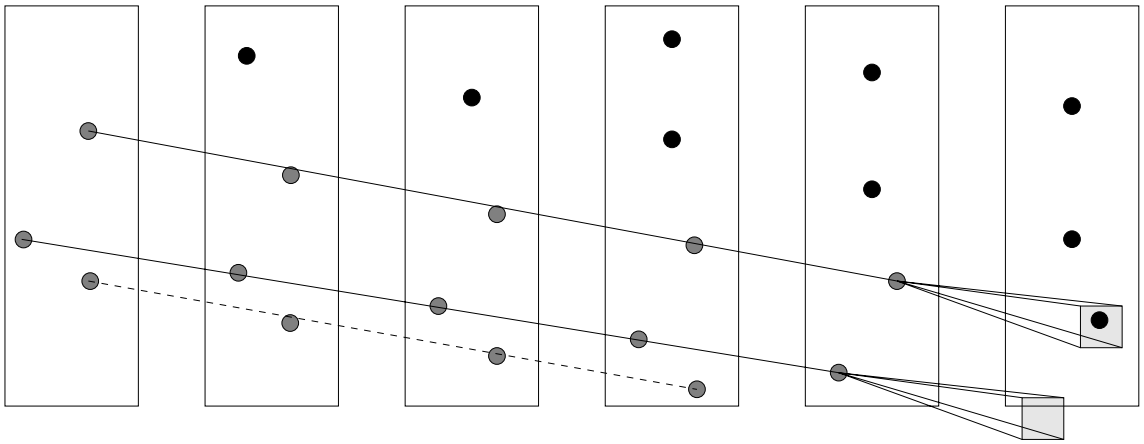

Figure E.1: Step 1: Predict the position of each drop.

3. Every centroid in the current image that is found correctly (in one to one correspondence with one "known" drop) is added to the trajectory on the "known" drop, and is removed from further consideration. Every drop which is not correctly found in the current image is eliminated from the list of "known" drops and passed to the analysis code.

4. The remaining centroids from the current image are added to the buffer.

5. Using the data in the buffer, all possible combinations of 5 consecutive centroids (as shown in Figure E.3 are hypothesized to be the trajectory of a drop. This trajectory is then checked for physical consistency. If the trajectory is satisfactory, the 5 centroids are removed from the buffer, and the data is used to add a new "known" drop to the list.

The details of the algorithm are consistent with the low artifact rate required, and available computational speed. Step 3 in the algorithm is very conservative— an apparent collision between a drop and any centroid causes the drop to be eliminated from the list (without the final, suspect centroid). Step 5 incorporates hashing techniques and an optimized search order through the list of possible trajectories in order to minimize the combinatorics involved in "all possible combinations". In order to prevent any given drop from entering the data sample twice, the trajectories found in Step 5 are constrained to have an initial point near the top of the field of view.

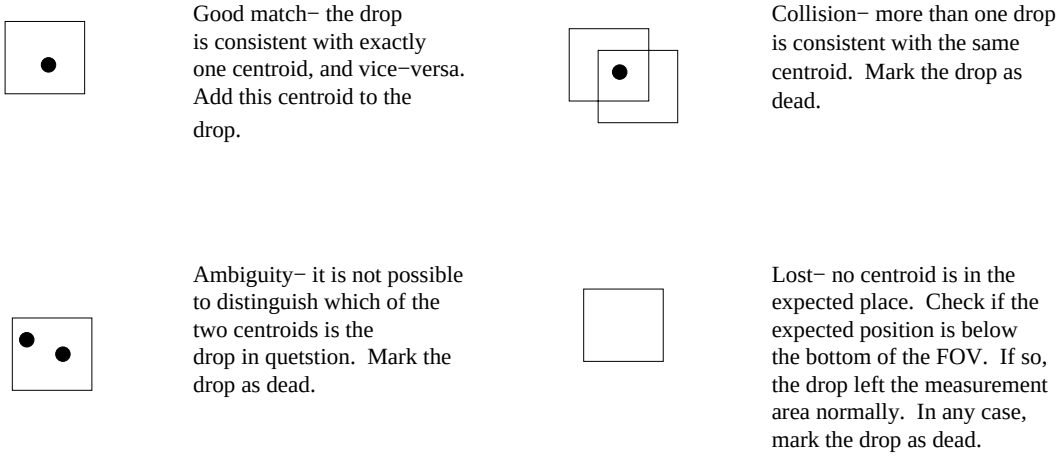

Figure E.2: Step 2: Look for centroids in the predicted positions

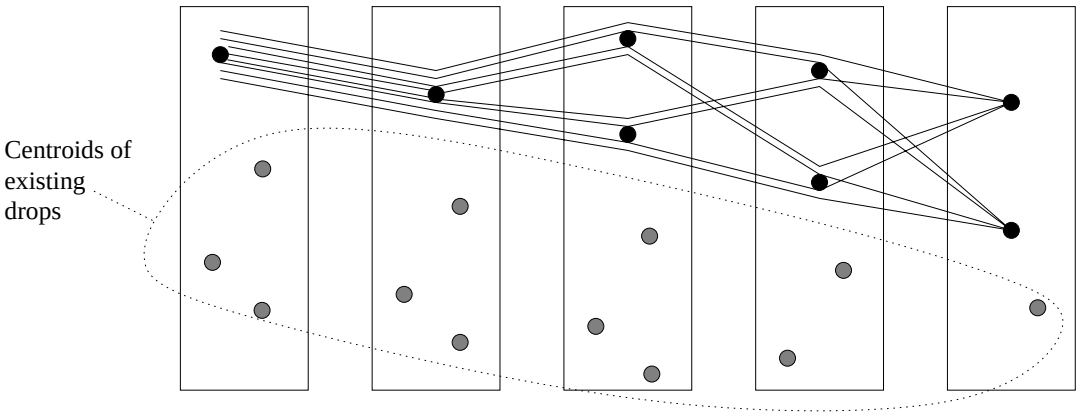

Figure E.3: Step 5: Test all possible combinations of unused centroids for physical consistency

A handful of adjustable parameters are necessary to control the tolerances in Step 3 and Step 5, and to minimize the statistical possibility that an incorrect combination in Step 5 will be found to be satisfactory.

The algorithm has achieved efficiencies in excess of 99.9%, and has been tested using Monte Carlo techniques to have a sufficiently low artifact rate. Very high drop rates, such that there are over 40 centroids per image are possible, but the limiting factor becomes statistical issues in Step 5. The algorithm is also easily capable of on-line operation at such rates. Hence, the experiment is not currently limited by tracking or computation issues.

Appendix F

Limitations of the method

Three are several ways in which the mass per second search rate can be increased in this experimental method.

F.1 Use of larger drops

The first way to increase the search rate is to use larger drops. Maintenance of the precision of the charge measurement requires that N_{images} increase in proportion to the drop radius. An increase in N_{images} can be accomplished by some combination of a decrease in v_z and an increase in the vertical length Z, Eq. (2.4). However a significant decrease in v_z requires too fine a balance between v_{air} and r^2, Eq. (2.3). If we keep v_z constant, an increase of Z can be attained by an increase in the number of vertical direction pixels in the CCD array of the camera. Existing CCD cameras with 10 Hz frame reading rates have twice the 736 vertical pixels used in the present camera and larger arrays will probably be available in the future. Therefore based on this consideration alone, drop diameters of several times 20 μm are feasible.

However, there are two problems that must be considered for drop diameters larger than 30 to 40 μm. The dipole force on a drop in a non-uniform electric field is proportional to the third power of the drop diameter. This force was negligible in this experiment, Sec. 5.3, but would have to be considered for much larger drops. The other problem is that the maintenance of a small and constant v_z, Eq. (2.3), requires

v_{air} to increase as the square of the drop diameter, possibly leading to non-laminar flow. Therefore without more design and experimental studies, our conservative conclusion is that the drop diameter is limited to about 30 μm. This would lead to an increase of the mass search rate by a factor of 3 compared to the 20 μm drops used in this experiment.

F.2 Increase of drop production rate per column of drops

Let the drop production rate for a column of drops be n per second. Then the vertical separation between drops in a column is $R = v_{air}/n$. The criteria in Sec. 6.1.6 require $R > 0.62$ mm. Using $v_{air} = 2.0$ mm/s, this gives an upper limit on n of about 3 Hz. However our experience in this experiment, Sec. 2.3, strongly suggests that a maximum 1 Hz rate is conservative practice, because of irregularities in drop production.

F.3 Increase in the number of drop columns

In this experiment we used one column of drops, however the extension to many columns of drops is straightforward. Of course the horizontal separation between adjacent columns must meet the requirements of Eq. (6.5), a nominal separation of 1 mm is useful for design purposes. The use of multiple columns requires two changes in the experimental design, namely the number of pixels in the horizontal direction in the CCD array must be increased and the space between the electric field plates must be increased. The latter requirement means the alternating potential applied across the plates must also be increased to keep the electric field constant.

Existing 10 Hz frame rate CCD cameras limit the number of columns to three but improvements in these cameras would probably allow five columns. The corresponding increase in the electric plate spacing and the potential difference is straightforward.

F.4 Correction for drop to drop interactions

It is clear that the primary constraint limiting the density of drops achievable in the measurement chamber is that of Eq. (6.5). To reiterate, interaction between the drops due to their induced electric dipole moment and viscous coupling requires that there be a minimum separation allowable between drops. In the limit that these interactions are small, both of these effects can be calculated from first principles, for example as in Eq. (6.4). In principle then, it should be possible to subtract the effect of these perturbing forces from the measured trajectory of each drop. Given this, it would be possible to relax the constraint on R. Since this possibility requires further study, it is not clear to what extent R can be reduced and throughput increased.

F.5 Summary

Putting these estimates together we can see how to achieve an improvement on the order of 10 times the present mass per second search rate using existing CCD cameras. Future cameras will probably allow a factor of 15 improvement.

Bibliography

[1] T. E. Faber. *Fluid Dynamics for Physicists*. Cambridge University Press, 1997.

[2] V. Halyo, P. Kim, E.R. Lee, I.T. Lee, D. Loomba, and M.L. Perl. Search for free fractional electric charge elementary particles using an automated millikan oil drop technique. *Physical Review Letters*, 84(12):2576–2579, March 20 2000.

[3] V.D. Hopper and T.H. Laby. The electronic charge. *Physics Reports*, 178(974):243–272, July 31 1941.

[4] W. G. Jones, P. F. Smith, G. J. Homer, J. D. Lewin, and H. E. Walford. Searches for fractional electric charge in meteorite samples. *Zeitschrift für Physik C*, 43:349–355, 1989.

[5] W.B. Kunkel. Charge distribution in coarse aerosols as a function of time. *Journal of Applied Physics*, 21:833–837, August 1950.

[6] W.B. Kunkel. The static electrification of dust particles on dispersion into a cloud. *Journal of Applied Physics*, 21:820–832, August 1950.

[7] W. E. Langlois. *Slow Viscous Flow*. The Macmillan Company, 1964.

[8] George S. LaRue, James D. Phillips, and William M. Fairbank. Observation of fractional charge of $(\frac{1}{3})$e on matter. *Physical Review Letters*, 46(15):967–970, April 13 1981.

[9] E.R. Lee and M.L. Perl. U.s. patent 5,943,075, August 24 1999. Assigned to Stanford University.

[10] Dinesh Loomba, Valerie Halyo, Eric R. Lee, Irwin T. Lee, and Peter C. Kim. A new method for searching for free fractional charge particles in bulk matter. *Review of Scientific Instruments*, 71(9):3409–3414, September 2000.

[11] Nancy M. Mar, Eric R. Lee, George R. Fleming, Brendan C.K. Casey, Martin L. Perl, and Edward L. Garwin. Improved search for elementary particles with fractional electric charge. *Physical Review D*, 53(11):6017–6032, June 1 1996.

[12] M. Marinelli and G. Morpurgo. The electric neutrality of matter: a summary. *Physics Letters B*, 137B(5,6):439–442, April 5 1984.

[13] William H. Press, Saul A. Teukolsky, William T. Vetterling, and Brian P. Flannery. *Numerical Recipes in C.* Cambridge University Press, 1992.

[14] Maureen L. Savage, Roger W. Bland, Christopher L. Hodges, Judith L. Huntington, David C. Joyce, Robert T. Johnson, Tanya D. Knoop, Michael A. Lindgren, Marion H. Scholz, Alan B. Steiner, and Betty A. Young. A search for fractional charges in native mercury. *Physics Letters B*, 167B(4):481–484, February 20 1986.

[15] P.F. Smith, G.J. Homer, J.D. Lewin, and H.E. Walford. A search for fractional electric charge on levitated niobium spheres. *Physics Letters B*, 153B(3):188–194, March 28 1985.